University of Crete
Department of Physics

Thesis submitted for the Master in Advanced Physics

Theoretical model fits to the optical/UV spectral energy distributions of AGN

Marios Papoutsis

Supervisor : Iossif Papadakis

Crete, June 2023

Contents

Chapter 1: Introduction **2**
1.1 The "big blue bump" . . . 2
1.2 Objective of our work . . . 4

Chapter 2: Accretion disk structure **5**
2.1 Radial disk structure . . . 5
2.2 Vertical disk structure . . . 7
2.2.1 Vertical pressure balance . . . 7
2.2.2 Energy generation . . . 7
2.2.3 Energy transport . . . 8
2.2.4 Equation of state . . . 8
2.3 Determination of the disk model parameters . . . 9
2.3.1 Inner region: $P = P_{rad}$, and $\bar{\kappa}_R = \kappa_{es}$ . . . 9
2.3.2 Middle region: $P = P_{gas}$, and $\bar{\kappa}_R = \kappa_{es}$ . . . 10
2.3.3 Outer region: $P = P_{gas}$, and $\bar{\kappa}_R = \overline{\kappa}_{ff}$ . . . 10

Chapter 3: Models for the disk spectral energy distribution **11**
3.1 The modified blackbody spectrum . . . 11
3.2 The color-corrected blackbody spectrum . . . 12
3.2.1 The Done et al. approach (D12) . . . 13
3.2.2 The Davis & El-Abd 2019 approach (DE19) . . . 13
3.3 Calculation of the disk spectrum . . . 15

Chapter 4: Fitting the spectral energy distribution of quasars **19**
4.1 The observed AGN SEDs . . . 19
4.2 Fitting method . . . 20
4.3 Results . . . 22
4.3.1 Best fits to the mean SED of quasars . . . 22
4.3.2 Best fits to the mean SEDs of low, mid, and high luminosity quasars . . . 26

Chapter 5: Summary and conclusions **32**

Appendices **34**
Appendix A: Derivation of disk's inner region parameters . . . 34
Appendix B: Computation of disk's surface temperature . . . 35

Bibliography **37**

Chapter 1: Introduction

An active galactic nucleus (AGN) is the central region of a galaxy where we observe energetic phenomena that cannot be attributed directly to stars. At least $\sim 10\%$ of galaxies in the near universe host AGN. Their luminosity can range from $\sim 10^{42}$erg s^{-1} to $\sim 10^{47}$erg s^{-1}, while the luminosity of a typical galaxy is about $\sim 10^{44}$erg s^{-1}.

AGN show broadband emission, that extends from radiowaves to γ-rays, with comparable amount of energy being emitted at all wavelengths. Another important observational property of AGN is the emission of strong lines (i.e. lines with large equivalent width), which can be very broad. This implies that the line emitting gas cloud move with velocity up to $5 \times 10^3 - 10^4$km s^{-1}.

AGN are highly variable, i.e. their luminosity changes significantly with time. AGN are variable in every waveband they have been observed. The time-scale and the amplitude of the observed variations decrease and increase, respectively, with increasing frequency. This feature can be used to set constraints on the size of the central nucleus as follows: assume that the flux doubles at a timescale of $t \sim 10^4$s (usual timescale for X-ray variability). This significant increase in brightness must involve some significant variation in the properties of the source as a whole. This means that the source cannot be larger than the variability time-scale multiplied by the speed of light, so that the physical process respinsible for the variation can travel through the whole source. This results in a size of $R \sim ct = 3 \times 10^{14} cm$ (or $\sim$0.01pc). This is surprisingly small for such bright sources. Similar considerations in the optical/UV band (where most of the luminosity is emitted) imply a source size of the order of a few light days.

The small size of the central engine in active galaxies, as well as the enormous amount of power that they emit, pause significant challenges in our understanding of how AGN work. We currently believe that the engine in AGN comprises of a supermassive black hole (SMBH) and an accretion disk around it. As the gas moves inwards, large amount of gravitational energy is released and heats the disk, which then emits optical/UV light. Regarding the disk formation, assume a number of gas clouds around the SMBH, each one with some velocity and angular momentum. As the gas clouds approach the black hole, due to the gravitational attraction that it exerts upon them, they will collide with each other. As a result, their bulk motion is slowed down, they get mixed up and orbit around the black hole, forming a disk. The direction of their rotation is decided by their initial total angular momentum. If we further assume that a form of viscosity (i.e. friction) exists in the disk, then the angular momentum can be redistributed among the gas particles. This allows most of them to spiral inwards, thus creating an accretion disk. The amount of energy that can be extracted from material spiraling towards the SMBH is equal to the binding energy of the innermost stable circular orbit (ISCO). For a non-rotating black hole approximately 6% of the rest mass energy can be extracted. This amount can increase to 40% for a rotating black hole, in which case the ISCO moves closer to the black hole. The energy that is released is dissipated to the gas as heat, due to viscosity, and is ultimately radiated away.

1.1 The "big blue bump"

The presence of the accretion disk is strongly supported by the observed optical/UV spectrum of AGN. Figure 1 shows flux measurements of tens of thousands of quasars, selected from the Sloan Digital Sky Survey (SDSS), (Figure taken from Krawczyk et al. 2013). Points with different colours indicate measurements with different filters (details can be found in Figure 8 of Krawczyk et al. 2013). The solid black line in Fig. 1 shows the mean spectral energy distribution (SED), i.e. the power emitted as a function of the frequency (or the wavelength) of radiation, using the measurements of the individual sources. The solid green line in the same figure shows the SED of a typical elliptical galaxy. The peak of the emission of the elliptical galaxy is at $\sim 1\mu$m. The

emitted power at higher frequencies decreases since the fraction of young, high temperature stars over the total number of stars is relatively small in normal galaxies. Such a trend of decreasing power in the UV band is observed in the SED of all normal galaxies. On the contrary, the AGN SED increases at wavelengths shorter than 1μm. In fact, Figure 1 shows that the peak of the AGN emission may happer at wavelengths as short as $\sim 1000\AA$ (or even shorter as absorption of UV radiation by interstellar hydrogen clouds in our galaxy makes it difficult to find the exact location of the peak). The increase of the emitted power of AGN with increasing frequency in the optical and UV bands is called the "big blue bump". It is a defining characteristic of AGN and one of the major differences between active and normal galaxies.

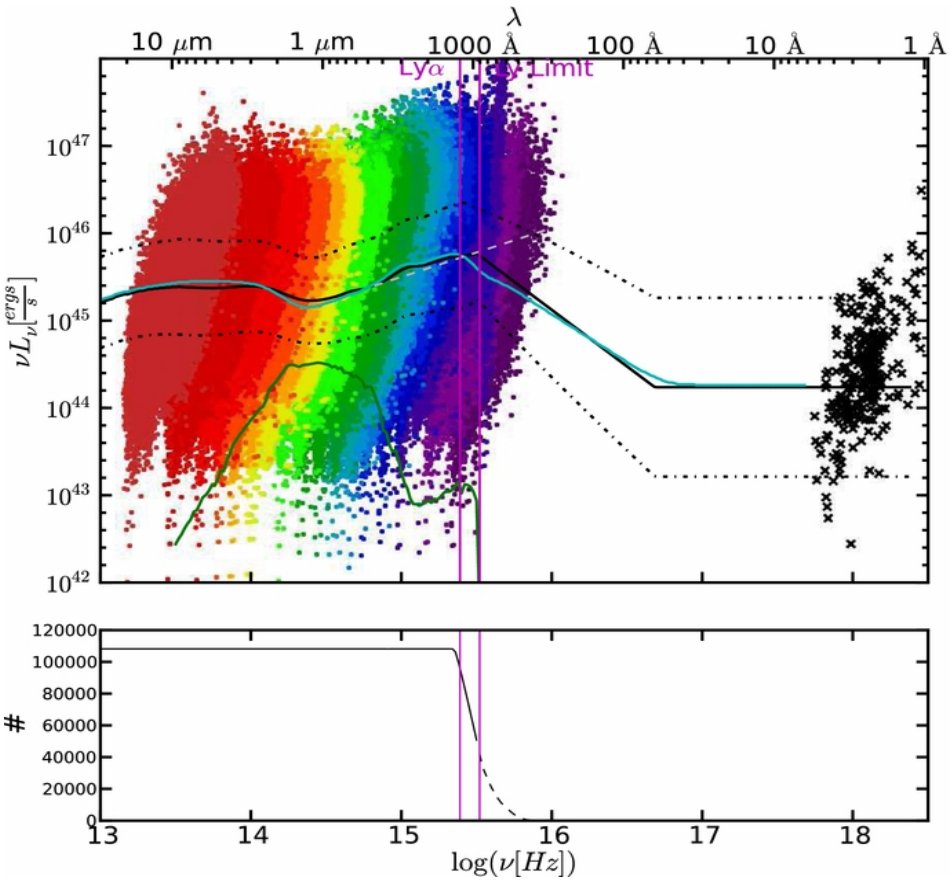

Figure 1: The colour scattered points show flux measurements in various filters, from tens of thousands of quasars. The solid black line shows the mean SED of these quasars, while the green solid line shows the SED of a typical elliptical galaxy (Figure taken from Krawczyk et al. 2013).

The big blue bump provides one the most challenging tests for the accretion-powered theory of AGN. There has been a lot of work in modeling the observed optical/UV SED of AGN. Most models adopt the ideas of Shakura & Sunyaev (1973; SS73 hereafter) who studied the structure and spectrum of geometrically thin and optically thick accretion disks. General relativistic effects were introduced by Novikov & Thorne (1973; NT73 hereafter). Significant improvements followed by considering radiative transfer in the disk atmosphere and disk winds (e.g. Hubeny et al. 2001, Davis & Laor 2011).

The SS73 and NT73 accretion disk models are relatively easy to compute and it is rather straightforward to fit the model spectra to observed SEDs. Many attempts have been done in the past to fit model disk spectra to AGN SEDs, with mixed conclusions. For example, Shang et al.

(2005) and Capellupo et al. (2015) studied the spectra of 17 and 30 AGN, respectively, and they found that thin accretion disk models can fit the data rather well. On the other hand, Davis et al. (2007), who measured the rest-frame far-UV and near-UV spectral slopes for thousands of AGN, and Jin et al. (2012), who fitted the spectra of ~ 50 SDSS AGN, find that the thin disk models do not fit the data well. Davis et al. (2007) claim that intrinsic reddening may be the cause of much of the discrepancy between models and observation, while Jin et al. claim that "warm" skin on top of the disk ("warm corona") and a hot X-ray emitting inner flow, maybe necessary to explain the data.

1.2 Objective of our work

The purpose of this work is to study simple theoretical models of the accretion disk in AGN, compute the resulting model SED, and then compare it with observed SEDs. We consider the NT73 model and we take into account the effects of electron opacity, i.e. Thomson scattering and free-free absorption, as well as Compton scattering. Regarding the first two processes, we consider the case of a modified blackbody spectrum, while regarding the latter process we consider the case of a colour correction to the blackbody emission formula. We then create model accretion disk spectra for a wide range of AGN parameters (i.e. black hole mass, accretion rate, spin, and inclination) and fit their average to the observed mean SED of 119,652 SDSS quasars (taken from Krawczyk et al. 2013). In this way, we can investigate whether the current accretion disk models are consistent with the observed AGN SED, and at the same time determine the bet-fit black hole mass, accretion rate, spin, and inclination distribution for a large sample of AGN. The sample size is one of the main differences between our modeling and previous works. In addition, we use a rather innovative way of accounting for the electron opacity effects and also include the relativistic effects of photon propagation from the disk to the observer at infinity as computed by Dovčiak (2004).

In Chapter 2, we introduce the radial and vertical structure equations for a general relativistic thin accretion disk (as was done by NT73), and write down the formulas for the disk pressure, density, height and temperature, as they are important for the calculation of the disk spectrum. In Chapter 3, we compute the disk SED assuming different emission cases: pure blackbody emission, color-corrected blackbody emission using the prescriptions of Done et al. (2012) and Davis & El-Abd (2019), and modified blackbody emission. In Chapter 4, we fit the mean observed SEDs of quasars as determined by Krawczyk et al. (2013), using model disk spectra for a wide range of AGN parameters (i.e. black hole mass, accretion rate, spin, inclination angle). We present our best-fits and the corresponding distributions of AGN parameters in sectrion 4.3. In Chapter 5, we summarize our results.

Chapter 2: Accretion disk structure

2.1 Radial disk structure

A general relativistic (GR) analysis for the structure of a thin accretion disk was performed by NT73. They considered a Kerr spacetime around a spinning black hole (BH) of mass M and accretion rate $\dot{M}$. They solved the equations of conservation of rest mass, conservation of angular momentum, and conservation of energy in the disk, and showed that the power per unit surface area dissipated to the disk due to frictional heating is equal to

$$Q_{GR}(R) = \frac{3}{8\pi}\frac{GM\dot{M}}{R^3}\frac{\mathcal{L}}{\mathscr{B}\mathscr{C}^{1/2}} \text{ (erg s}^{-1}\text{ cm}^{-2}), \tag{1}$$

where G is the gravitational constant, R the radial distance from the black hole, and $\mathscr{B}, \mathscr{C}, \mathcal{L}$ are relativistic corrections given below

$$\mathscr{B} = 1 + \alpha^*/r^{3/2} \ , \tag{2}$$

$$\mathscr{C} = 1 - 3/r + 2\alpha^*/r^{3/2} \ , \tag{3}$$

$$\begin{aligned}\mathcal{L} = \frac{1+\alpha^* x^{-3}}{(1-3x^{-2}+2\alpha^* x^{-3})^{1/2}}\frac{1}{x}\Big[x - x_0 - \frac{3}{2}\alpha^*\ln(\frac{x}{x_0}) - \frac{3(x_1-\alpha^*)^2}{x_1(x_1-x_2)(x_1-x_3)}\ln(\frac{x-x_1}{x_0-x_1}) \\ -\frac{3(x_2-\alpha^*)^2}{x_2(x_2-x_1)(x_2-x_3)}\ln(\frac{x-x_2}{x_0-x_2}) - \frac{3(x_3-\alpha^*)^2}{x_3(x_3-x_1)(x_3-x_2)}\ln(\frac{x-x_3}{x_0-x_3})\Big] \ ,\end{aligned} \tag{4}$$

where eq.(4) is taken from Page and Thorne (1973). The dimensionless parameters introduced in the above equations are: $r \equiv R/R_g$, where $R_g = GM/c^2$ is the gravitational radius, the dimensionless spin parameter of the black hole α^* $(0 \leq \alpha^* \leq 1)$, [1] and the radial coordinate $x = \sqrt{r}$. Parameters x_1, x_2, x_3 are the roots of the equation $x^3 - 3x + 2\alpha^* = 0$ ($x_1 = 2\cos(\frac{1}{3}\cos^{-1}\alpha^* - \pi/3)$, $x_2 = 2\cos(\frac{1}{3}\cos^{-1}\alpha^* + \pi/3)$ and $x_3 = -2\cos(\frac{1}{3}\cos^{-1}\alpha^*)$), and $x_0 = \sqrt{r_{ms}}$ where r_{ms} is the radius of the marginally stable orbit (also called innermost stable circular orbit) in units of R_g given by

$$r_{ms} = 3 + Z_2 - [(3-Z_1)(3+Z_1+2Z_2)]^{1/2} \ , \tag{5}$$

$$Z_1 = 1 + (1-a_*)^{1/3}[(1+a_*)^{1/3} + (1-a_*)^{1/3}] \ , \tag{6}$$

$$Z_2 = (3a_*^2 + Z_1^2)^{1/2} \ . \tag{7}$$

For a non-rotating black hole ($\alpha^* = 0$) eq.(5) gives $r_{ms} = 6$, as expected, while for a maximally rotating black hole (α^*=1) we find $r_{ms} = 1$.

The Newtonian version of eq.(1), i.e.

$$Q_N(R) = \frac{3}{8\pi}\frac{GM\dot{M}}{R^3}(1 - \sqrt{\frac{6R_g}{R}}) \text{ (erg s}^{-1}\text{ cm}^{-2}), \tag{8}$$

is also often found in the literature.

An important assumption of both eq.(1) and eq.(8) is that no viscous stresses can act on the surface $r = r_{ms}$. This is reasonable since at $r < r_{ms}$ the gas will spiral rapidly into the black hole and thus the gas density of this region is insignificant compared to that at $r > r_{ms}$. In the remainder of this section, we plot Q_{GR}, and Q_N.

[1] The dimensionless spin parameter is defined as $\alpha^* = Jc/GM^2$, where J is the angular momentum of the black hole.

Let us consider the dimensionless parameters for the radius, the mass, and the accretion rate:

$$r = \frac{R}{R_g} \ , \ M_8 = \frac{M}{10^8 M_\odot} \ , \ \dot{m} = \frac{\eta \dot{M} c^2}{L_{edd}} \ , \tag{9}$$

where L_{edd} is the Eddington luminosity given by

$$L_{edd} = \frac{4\pi G M m_p c}{\sigma_T} = 1.26 \times 10^{38} \frac{M}{M_\odot} \ (\text{erg/sec}) \ , \tag{10}$$

with m_p being the proton mass, σ_T the Thomson scattering cross section and η is the spin dependent efficiency of accretion (e.g. for spin $\alpha^* = 0$ we have $\eta = 0.057$ [2]) . Using these parameters eq.(1) and eq.(8) become

$$Q_{GR}(r) = 7 \times 10^{18} \frac{(\dot{m}/\eta)}{M_8} r^{-3} \frac{\mathcal{L}}{\mathscr{B}\mathscr{C}^{1/2}} \ , \tag{11}$$

$$Q_N(r) = 7 \times 10^{18} \frac{(\dot{m}/\eta)}{M_8} r^{-3} (1 - \sqrt{\frac{6}{r}}) \ . \tag{12}$$

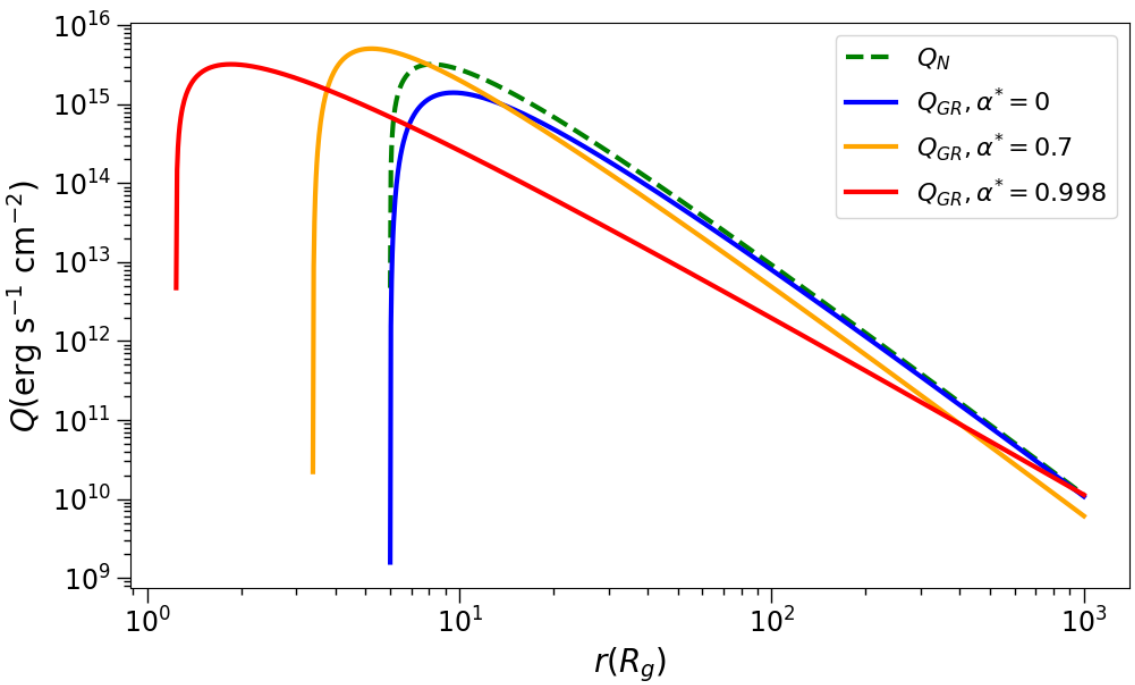

Figure 2: Power per unit surface area dissipated to the disk due to frictional heating for the case of $M_8 = 1$, $\dot{m} = 0.1$. The dashed green line shows the Newtonian case, $Q_N(r)$, and the solid blue, orange, and red lines show the general relativistic case, $Q_{GR}(r)$, for α^*=0, 0.5, 0.998 respectively.

The solid blue and dashed green lines of Figure 2 show $Q_{GR}(r), Q_N(r)$ as a function of r for the case of $M_8 = 1$, $\dot{m} = 0.1$, α^*=0. The solid orange and solid red lines show $Q_{GR}(r)$ for the same $M_8, \dot{m}$ and for α^*=0.7 and 0.998 respectively. They are calculated at $N_r = 1000$ radii which are equidistant in the log space, i.e.

$$\log(r_i) = \log(r_{ms}) + i \frac{[\log(r_{out}) - \log(r_{ms})]}{N_r} \ , \tag{13}$$

[2]The efficiency is equal to $\eta = 1 - U_t(r_{ms})$, where $U_t(r_{ms}) = \frac{4(\sqrt{r_{ms} - \alpha^*}) + \alpha^*}{\sqrt{3} r_{ms}}$ is the four-velocity of the accreting matter at ISCO.

where $r_{out} = 1000$ is the outer edge of the disk.

As radius decreases, the power dissipation per unit surface area increases. This happens because more gravitational energy is released at the inner parts of the disk. As the value of α^* increases the marginally stable orbit moves closer to the black hole, and thus Q reaches even higher values there. However, if we compare Q for different spins at the same radius (e.g. r=10) we see that as spin increases Q decreases. This happens since $\dot{m}$ depends on the efficiency of accretion. For larger values of spin, η becomes larger as well. It is due to that enhanced efficiency that the accretion rate in physical units decreases (for the same value of $\dot{m}$), and thus Q decreases as well. At large radii ($r \sim 1000$), all the different lines give similar values since most of the dissipation happens close to the inner edge of the disk. It is interesting to compare the Q_{GR} with Q_N when α^*=0. In both cases, the innermost stable circular orbit is at 6 R_g. However, the power per surface area dissipated in the general relativistic case is noticeably smaller than the one of the Newtonian case close to r_{ms}.

2.2 Vertical disk structure

For some emission cases, knowing the power dissipated per surface area due to viscous heating is not enough information to compute the disk spectrum. We also have to calculate the disk's density $\rho(R, z)$, where z is the height from the disk midplane. To do this, we need a detailed model of the disk's vertical structure, i.e. a set of equations for the vertical structure parameters of the disk: $\rho(R, z)$, pressure $P(R, z)$, internal temperature $T(R, z)$, flux of energy $F(R, z)$, shear stress $t(R, z)$ and Rosseland mean opacity $\bar{\kappa}(R, z)$. In this section, we write down these equations and solve them by approximating the vertical structure parameters with their mean values in the disk interior.

2.2.1 Vertical pressure balance

The equation of hydrostatic equilibrium for a vertically thin disk is given by

$$\frac{1}{\rho}\frac{dP}{dz} = \text{“acceleration of gravity”} = -\frac{GMz}{R^3}\frac{\mathscr{B}^2\mathscr{D}\mathscr{E}}{\mathscr{A}^2\mathscr{C}} \ , \tag{14}$$

where $\mathscr{A}, \mathscr{D}, \mathscr{E}$ are relativistic correction factors (like the ones introduced in section 2.1) given by

$$\mathscr{A} = 1 + a_*^2/r^2 + 2a_*^2/r^3 \ , \tag{15}$$

$$\mathscr{D} = 1 - 2a_*^2/r + a_*^2/r^2 \ , \tag{16}$$

$$\mathscr{E} = 1 + 4a_*^2/r^2 - 4a_*^2/r^3 + 3a_*^4/r^4 \ . \tag{17}$$

By approximating P and ρ with their average values in the disk interior and setting $z = H$ on the right-hand side of eq.(14), where H is the disk height, eq.(14) becomes

$$P = \rho\frac{GM}{R^3}H^2\frac{\mathscr{B}^2\mathscr{D}\mathscr{E}}{\mathscr{A}^2\mathscr{C}} \ . \tag{18}$$

2.2.2 Energy generation

The generation of the energy flux F(erg s^{-1} cm^{-2}) flowing out of the upper surface of the disk is

$$\frac{dF}{dz} = \frac{3}{2}(\frac{GM}{R^3})^{1/2}t\frac{\mathscr{D}}{\mathscr{C}} \ . \tag{19}$$

To progress this expression further we need an assumption for the shear stress t caused by viscosity. We assume that

$$t = aP \ , \tag{20}$$

where a is the viscosity parameter ($0 \leq a \leq 1$). NT73 approximate F by a mean value of $Q_{GR}/2$. Then eq.(19) becomes

$$Q_{GR} = 3a(\frac{GM}{R^3})^{1/2} HP \frac{\mathscr{D}}{\mathscr{C}} \ . \tag{21}$$

2.2.3 Energy transport

Assuming that the energy transport through the disk is due to radiative diffusion, we can use the Rosseland approximation for the disk flux radiated away, i.e.

$$F(z) = -\frac{16\sigma T^3}{3\alpha_R} \frac{\partial T}{\partial z} \ , \tag{22}$$

where σ is the Stefan–Boltzmann constant, α_R is the Rosseland mean absorption coefficient, which is a weighted average of the absorption and scattering coefficients over all frequencies, and is equal to $\alpha_R = \rho\bar{\kappa}$. Approximating with the average value of T in the disk midplane we find

$$F = \frac{4\sigma}{3\rho H \bar{\kappa}_R} T^4 \ . \tag{23}$$

We assume that the main opacity contributions come from free-free transitions and Thomson scattering (we ignore line opacity and bound-free transitions). The Rosseland mean opacity in this case has the form

$$\bar{\kappa}_R = \overline{\kappa}_{ff} + \kappa_{es} \ , \tag{24}$$

where κ_{es} is the Thomson scattering opacity and $\overline{\kappa}_{ff}$ the free-free opacity averaged over all frequencies, given below

$$\kappa_{es} = 0.4 \ (\mathrm{cm}^2 \ \mathrm{g}^{-1}) \ , \tag{25}$$

$$\overline{\kappa}_{ff} = 6.4 \times 10^{22} \rho T^{-7/2} \ (\mathrm{cm}^2 \ \mathrm{g}^{-1}) \ . \tag{26}$$

2.2.4 Equation of state

The pressure in the disk is due to gas and radiation (we ignore turbulent pressure and pressure due to magnetic fields). Assuming ideal gas, we have

$$P_{gas} = nkT \ , \tag{27}$$

where n is the number of particles per unit volume and k is the Boltzmann constant. We can use $n = \rho/\mu m_p$ to eliminate n and get

$$P_{gas} = \frac{\rho kT}{\mu m_p} \ , \tag{28}$$

where μ is the mean mass per particle measured in units of hydrogen mass m_H. It is called the mean molecular mass, and is equal to 1 for neutral hydrogen, while for ionized hydrogen it is equal to 1/2. In our case, we will use $\mu = 1/2$.

The radiation pressure is, assuming black body radiation,

$$P_{rad} = \frac{4\sigma T^4}{3c} \ . \tag{29}$$

Therefore the total pressure is

$$P = \frac{2\rho kT}{m_p} + \frac{4\sigma T^4}{3c} \ . \tag{30}$$

2.3 Determination of the disk model parameters

By combining the equation of radial disk structure for Q_{GR} and the approximate equations for the vertical structure we have the following set of equations

$$P(R) = \rho \frac{GM}{R^3} H^2 \frac{\mathscr{B}^2 \mathscr{D} \mathscr{E}}{\mathscr{A}^2 \mathscr{C}} \ , \tag{31}$$

$$Q_{GR}(R) = 3a(\frac{GM}{R^3})^{1/2} H P \frac{\mathscr{D}}{\mathscr{C}} \ , \tag{32}$$

$$F(R) = \frac{4\sigma}{3\rho H \bar{\kappa}_R} T^4 \ , \tag{33}$$

$$P(R) = \frac{2\rho k T}{m_p} + \frac{4\sigma T^4}{3c} \ . \tag{34}$$

If we assume that all the power that heats up the disk is radiated away, i.e. $F = Q_{GR}/2$, then we can solve the above set of equations and determine the 4 unknown disk parameters: ρ, P, T, H.

The analytical solution of the above equations is obtained by assuming that the disk can be divided into 3 regions: an inner region where the radiation pressure dominates over the gas pressure (i.e. $P \approx P_{rad}$) and the main contribution to opacity is Thomson scattering, a middle region where gas pressure dominates over radiation pressure (i.e. $P \approx P_{gas}$) and electron scattering is still the main opacity contribution, and an outer region where gas pressure dominates and the opacity is predominantly free-free. Next, we present the solutions in each region using the dimensionless parameters of $r, M_8, \dot{m}$ defined in eq.(9). The derivation of the inner region solutions is shown in Appendix A.

2.3.1 Inner region: $P = P_{rad}$, and $\bar{\kappa}_R = \kappa_{es}$

$$\rho = 2 \times 10^{-13} (aM_8)^{-1} (\dot{m}/\eta)^{-2} r^{3/2} \mathscr{A}^{-4} \mathscr{B}^6 \mathscr{D} \mathscr{E}^2 \mathcal{L}^{-2} \, (\mathrm{g\ cm^{-3}}) \ , \tag{35}$$

$$\frac{H}{R} = (\dot{m}/\eta) r^{-1} \mathscr{A}^2 \mathscr{B}^{-3} \mathscr{C}^{1/2} \mathscr{D}^{-1} \mathscr{E}^{-1} \mathcal{L}^1 \ , \tag{36}$$

$$T = 5 \times 10^5 (aM_8)^{-1/4} r^{-3/8} \mathscr{A}^{-1/2} \mathscr{B}^{1/2} \mathscr{E}^{1/4} \, (\mathrm{K}) \ , \tag{37}$$

$$P = P_{rad} = 2 \times 10^8 (aM_8)^{-1} r^{-3/2} \mathscr{A}^{-2} \mathscr{B}^2 \mathscr{E} \, (\mathrm{dyn\ cm^{-2}}) \ . \tag{38}$$

To identify the transition radius from the inner region to the middle one, we need to calculate the ratio of the gas pressure over the radiation pressure, i.e.

$$\frac{P_{gas}}{P_{rad}} = 4 \times 10^{-8} (aM_8)^{-1/4} (\dot{m}/\eta)^{-2} r^{21/8} \mathscr{A}^{-5/2} \mathscr{B}^{9/2} \mathscr{D} \mathscr{E}^{5/4} \mathcal{L}^{-2} \ . \tag{39}$$

The transition occurs when $P_{gas}/P_{rad} = 1$ which gives the following equation, that can be solved numerically for r,

$$r = 700 (aM_8)^{2/12} (\dot{m}/\eta)^{16/21} \mathscr{A}^{20/21} \mathscr{B}^{-36/21} \mathscr{D}^{-8/21} \mathscr{E}^{-10/21} \mathcal{L}^{16/21} \ . \tag{40}$$

2.3.2 Middle region: $P = P_{gas}$, and $\bar{\kappa}_R = \kappa_{es}$

$$\rho = 10^{-4}(aM_8)^{-7/10}(\dot{m}/\eta)^{2/5}r^{-33/20}\mathscr{A}^{-1}\mathscr{B}^{3/5}\mathscr{D}^{-1/5}\mathscr{E}^{1/2}\mathcal{L}^{2/5}\,(\mathrm{g\ cm^{-3}})\ , \tag{41}$$

$$\frac{H}{R} = 2\times 10^{-3}(aM_8)^{-1/10}(\dot{m}/\eta)^{1/5}r^{1/20}\mathscr{A}\mathscr{B}^{-6/5}\mathscr{C}^{1/2}\mathscr{D}^{-3/5}\mathscr{E}^{-1/2}\mathcal{L}^{1/5}\ , \tag{42}$$

$$T = 2\times 10^{7}(aM_8)^{-1/5}(\dot{m}/\eta)^{2/5}r^{-9/10}\mathscr{B}^{-2/5}\mathscr{D}^{-1/5}\mathcal{L}^{2/5}\,(\mathrm{K})\ , \tag{43}$$

$$P = P_{gas} = 3\times 10^{11}(aM_8)^{-9/10}(\dot{m}/\eta)^{4/5}r^{-51/20}\mathscr{A}^{-1}\mathscr{B}^{1/5}\mathscr{D}^{-2/5}\mathscr{E}^{1/2}\mathcal{L}^{4/5}\,(\mathrm{dyn\ cm^{-2}})\ , \tag{44}$$

2.3.3 Outer region: $P = P_{gas}$, and $\bar{\kappa}_R = \overline{\kappa}_{ff}$

The transition from the middle region to the outer one occurs when the optical depth due to free-free absorption becomes equal to the optical depth due to electron scattering, i.e., $\tau_{ff}/\tau_{es} = 1$. This ratio is equal to

$$\frac{\tau_{ff}}{\tau_{es}} = 210^{-3}(\dot{m}/\eta)^{-1/2}r^{3/4}\mathscr{A}^{-1/2}\mathscr{B}^{2/5}\mathscr{D}^{1/4}\mathscr{E}^{1/4}\mathcal{L}^{-1/2}\ , \tag{45}$$

so the radius at which the transition happens is given by

$$r = 5\times 10^{3}(\dot{m}/\eta)^{2/3}\mathscr{A}^{2/3}\mathscr{B}^{-8/15}\mathscr{D}^{-1/3}\mathscr{E}^{-1/3}\mathcal{L}^{2/3}\ . \tag{46}$$

For larger r the disk parameters become

$$\rho = 10^{-3}(aM_8)^{-7/10}(\dot{m}/\eta)^{11/20}r^{-15/8}\mathscr{A}^{-17/20}\mathscr{B}^{3/10}\mathscr{D}^{-11/40}\mathscr{E}^{17/40}\mathcal{L}^{11/20}\,(\mathrm{g\ cm^{-3}})\ , \tag{47}$$

$$\frac{H}{R} = 4\times 10^{-4}(aM_8)^{-1/10}(\dot{m}/\eta)^{3/20}r^{1/8}\mathscr{A}^{19/20}\mathscr{B}^{-11/10}\mathscr{C}^{1/2}\mathscr{D}^{-23/40}\mathscr{E}^{-19/40}\mathcal{L}^{3/20}\ , \tag{48}$$

$$T = 4\times 10^{6}(aM_8)^{-1/5}(\dot{m}/\eta)^{3/10}r^{-3/4}\mathscr{A}^{-1/10}\mathscr{B}^{-1/5}\mathscr{D}^{-3/20}\mathscr{E}^{1/20}\mathcal{L}^{3/10}\,(\mathrm{K})\ , \tag{49}$$

$$P = P_{gas} = 7\times 10^{11}(aM_8)^{-9/10}(\dot{m}/\eta)^{17/20}r^{-21/8}\mathscr{A}^{-19/20}\mathscr{B}^{1/10}\mathscr{D}^{-17/40}\mathscr{E}^{19/40}\mathcal{L}^{17/20}\,(\mathrm{dyn\ cm^{-2}})\ , \tag{50}$$

Chapter 3: Models for the disk spectral energy distribution

In this chapter, we are interested in computing the spectrum emitted by the accretion disk. This is usually done by splitting the disk into many narrow annuli, and assuming that each one emits approximately as a blackbody of constant temperature. Then, the contribution of each ring is summed up to create the full spectrum at some frequency. However, the blackbody is an idealization of a body that can absorb all the incident radiation and is at thermodynamic equilibrium with its environment, meaning that it emits as much radiation as it absorbs and has a constant temperature. This is not the case for physical objects like stars and accretion disks, since they are not in thermal equilibrium with the space around them. The disk temperature and density vary along the vertical direction z. Therefore, to compute the emergent spectrum we need to perform radiative transfer through the vertical structure at each radius, considering all the interactions between photons and matter, such as bound-free and free-free absorption, Thomson and Compton scattering.

A way to include some of these opacity effects while not having to deal with the full radiative transfer is to assume that each disk annulus emits as a modified blackbody or as a color-corrected blackbody. We explore these approaches in the next two sections.

3.1 The modified blackbody spectrum

A discussion on how Thomson scattering can modify the emitted spectrum so that it is no longer blackbody is made in NT73. Let y_ν be the depth (in units of g cm^{-2}) in the disk where photons are formed by free-free emission:

$$y_\nu = \int_{\text{formation point}}^{\infty} \rho dz \ . \tag{51}$$

Before these photons manage to escape the disk, they scatter with electrons. The mean free path for electron scattering is $\lambda = 1/\kappa_{es} = 2.5\text{g cm}^{-2}$. Then, the total depth traveled by the photons through random-walk before they escape is equal to their mean free path multiplied by the square root of the number of scatterings N_{es}

$$y_\nu = N_{es}^{1/2}/\kappa_{es} \ . \tag{52}$$

In the outer parts of the disk, where free-free absorption effects are dominant and electron scattering is negligible, the optical depth is

$$\tau_{ff} = \kappa_{ff} y_\nu = 1 \ . \tag{53}$$

Then $y_\nu \propto \kappa_{ff}^{-1} \propto \rho^{-1} T^{7/2}$. Using equations (47) and (49) for ρ, T in the outer disk region and ignoring the relativistic corrections (this is okay for the outer disk), we find $y_\nu \propto r^{-3/4}$. Then, eq.(52) gives $N_{es} \propto y_\nu^2 \propto r^{-3/2}$. As the radius decreases, the amount of scattering increases, and thus at some radius electron scattering becomes important. This has a strong effect on the emerging spectrum since only a fraction of the photons with blackbody intensity formed at y_ν will ever reach the disk surface. Most of them will be scattered back into depths greater than y_ν and eventually get absorbed there.

To model this effect we take the specific intensity of the disk at each frequency to be that of a modified black body, given by (Rybicki & Lightman, 1979)

$$I_\nu = \frac{4h\nu^3/c^2}{(e^{h\nu/kT_s} - 1)(1 + \sqrt{1 + \kappa_{es}/\kappa_{ff}})} (\text{erg s}^{-1}\ \text{cm}^{-2}\ \text{Hz}^{-1}\ \text{ster}^{-1}) \ , \tag{54}$$

where T_s is the disk surface temperature, and κ_{es}, κ_{ff} are the opacities for Thomson scattering and free-free absorption, respectively. Equation (54) is valid for a medium in which scattering,

absorption, and emission occur. It assumes that the medium is homogeneous and isothermal. This is a good approximation for each annulus of a thin disk because we take their width to be small. It further assumes that scattering is isotropic (which is a good approximation to the forward-backward symmetry of Thomson scattering). However, opacity effects of bound-free and bound-bound transitions are ignored. This approximation is reasonable at high temperatures ($>\sim 10^4 K$).

In the cases where Thomson scattering is negligible compared with free-free absorption, I_ν approaches the spectrum of a blackbody

$$B_\nu = \frac{2h\nu^3}{c^2}\frac{1}{e^{h\nu/kT_s}-1}(\text{erg s}^{-1}\text{ cm}^{-2}\text{ Hz}^{-1}\text{ sr}^{-1}). \tag{55}$$

On the other hand, when $\kappa_{es} \gg \kappa_{ff}$ the spectrum becomes that of a modified blackbody, i.e. $I_\nu = 2B_\nu\sqrt{\kappa_{ff}/\kappa_{es}}$. The opacity for electron scattering is given in eq.(25) and the frequency dependent free-free opacity is given below

$$\kappa_{ff} = 1.5\times 10^{25}\rho T_s^{-7/2}\frac{1-e^{-x}}{x^3}g(x,T_s)\ (\text{cm}^2\text{ g}^{-1})\ , \tag{56}$$

where $x = h\nu/kT_s$ and $g(x,T_s)\approx 1$ is the Gaunt factor. κ_{ff} depends strongly on the disk temperature and density. It also decreases with increasing frequency, which means that κ_{ff} may dominate the spectrum at low frequencies.

To compute the spectrum, using eq.(54), we need the surface temperature of the disk. This is obtained by equating the total emitted flux, i.e. the integral of I_ν over all frequencies and solid angles, to the total power emitted per unit surface area, i.e. Q_{GR}. We have

$$\pi\int_0^\infty I_\nu d\nu = Q_{GR}\ (\text{erg s}^{-1}\text{ cm}^{-2})\ . \tag{57}$$

Substituting the expressions for I_ν and Q_{GR} into the above equation we get

$$\frac{4\pi h}{c^2}\int_0^\infty \frac{\nu^3 d\nu}{(e^{h\nu/kT_s}-1)(1+\sqrt{1+\kappa_\tau/\kappa_{ff}})} = \frac{3}{8\pi}\frac{GM\dot{M}}{R^3}\frac{\mathcal{L}}{\mathscr{B}\mathscr{C}^{1/2}}\ . \tag{58}$$

We perform the change of variables $x\equiv h\nu/kT_s$, and use the dimensionless parameters $r, M_8, \dot{m}$ to find

$$4\pi\frac{k^4T_s^4(r)}{h^3c^2}\int_0^\infty \frac{x^3dx}{(e^x-1)[1+\sqrt{1+\kappa_{es}/\kappa_{ff}(x,\rho(r),T_s(r))}]} = 7\times 10^{18}\frac{(\dot{m}/\eta)}{M_8}r^{-3}\frac{\mathcal{L}}{\mathscr{B}\mathscr{C}^{1/2}} \tag{59}$$

This equation can be solved numerically for the surface temperature at each disk annuli (more information is given in Appendix B). Notice that to solve eq.(59) we need the disk density, which contains information about the vertical structure of the disk. After we know $T_s(r)$, we can calculate the *local* emission of each disk annuli. The calculation of the total spectrum is performed in section 3.3.

3.2 The color-corrected blackbody spectrum

At small radii the disk temperature increases significantly and thus Compton scattering may become important. In this case, the resulting spectra can be modeled by a color-corrected blackbody

$$I_\nu^{cc} = \frac{2h}{c^2f^4}\frac{\nu^3}{e^{h\nu/fkT_{eff}}-1}(\text{erg s}^{-1}\text{ cm}^{-2}\text{ Hz}^{-1}\text{ sr}^{-1})\ , \tag{60}$$

where f is known as the color correction or spectral hardening factor, and T_{eff} is the disk's effective temperature given by

$$T_{eff} \equiv (\frac{Q_{GR}}{\sigma})^{1/4} \ . \tag{61}$$

The presence of this factor in the exponential shifts the spectral features to higher energies. This means that the color-corrected blackbody can model the Wien tail at the high energy end of the spectrum, that is generally enforced by the inelastic scattering of electrons and photons (Shimura & Takahara 1995). However, this approach relies on having some method of computing f. We follow two such methods, as we describe below.

3.2.1 The Done et al. approach (D12)

Done et al. (2012) studied the Hubeny et al. (2001) accretion disk spectra, as recalculated in Davis & Hubeny (2006). Their disk models assume Novikov–Thorne emissivity and include full radiative transfer through the vertical structure of the disk at each radius. They also take into account both Compton scattering and metal opacities (bound– free transitions). Done et al. showed that the spectra calculated by the full radiative transfer code can be approximated by the spectrum defined in eq.(60), with

- $f = 1$ for $T_{eff} < 3 \times 10^4 K$,
- $f = [T_{eff}/(3 \times 10^4)]^{0.82}$ for $3 \times 10^4 < T_{eff} < 10^5$K, and
- $f = [72keV/kT_{eff}]^{1/9}$ for $T_{eff} > 10^5 K$,

where $k = 8.62 \times 10^{-8}$ keV K^{-1}. For low temperatures, blackbody emission is a good approximation to the true disk spectrum, i.e. $f = 1$, because electron scattering is less important and H starts to become neutral so the associated absorption edge opacity is large. In the critical temperature range $3 \times 10^4 < T_{eff} < 10^5$K, the color correction factor is higher since hydrogen and helium are ionized and Thomson scattering dominates. The f for higher temperature is assumed to model Compton scattering.

3.2.2 The Davis & El-Abd 2019 approach (DE19)

Davis & El-Abd (2019) studied the evolution of f with black hole mass and accretion rate by fitting color-corrected blackbody models to synthetic spectral models generated by the TLUSTY code (Hubeny 1990; Hubeny & Lanz 1995). They found that f displays a complicated variation with the effective temperature T_{eff}, the tidal gravity parameter g and the disk surface density parameter m_0 (also called midplane column mass), where

$$g \equiv \frac{GM}{R^3} \frac{\mathscr{B}^2 \mathscr{D} \mathscr{E}}{\mathscr{A}^2 \mathscr{C}} \ , \tag{62}$$

$$m_0 \equiv \frac{\Sigma}{2} = \rho H \ . \tag{63}$$

They studied f for log$g$ ranging from -10 to 11, in steps of 1 dex, logT_{eff} from 5 to 7.5 in steps of 0.1 dex, and log m_0 at values of 2.5, 2.75, 3, 4, 5, and 6. By restricting their parameter space to $m_0 \geq 10^3$g cm^{-2} and $0.01 < \dot{m} < 1$ they found that f can be approximated by

$$f = 1.74 + 1.06(\log T_{eff} - 7) - 0.14(\log g - 7) - 0.07(\log m_0 - 5) \ . \tag{64}$$

The effects of Compton scattering to the emitted disk spectrum can be modeled by dividing the disk into narrow annuli, calculating T_{eff}, g, and m_0 in each one of them and then using eq.(64) to compute f. However, this can be done as long as the disk parameters are within the parameter range that Davis & El-Abd (2019) had considered. To investigate this, we compute T_{eff}, g, m_0 for different cases of black hole masses and accretion rates and we plot them as a function of the radius in Figures 3, 4 and 5.

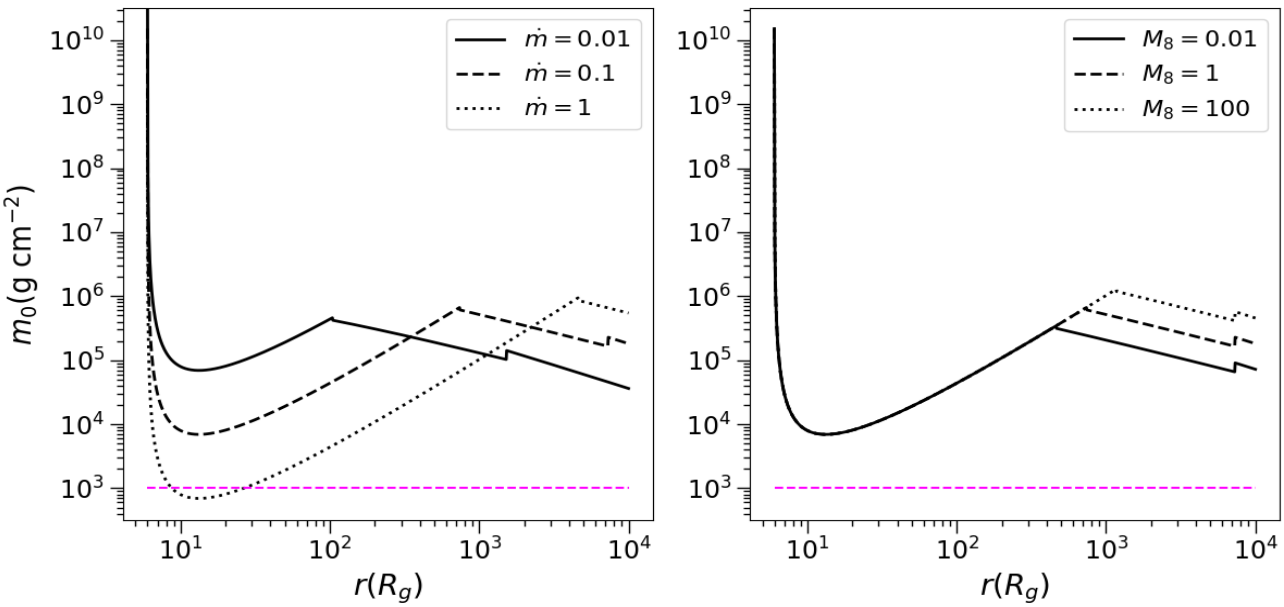

Figure 3: The surface density parameter m_0 as a function of the radius for black hole mass $M_8 = 1$ and accretion rates $\dot{m} = 0.01, 0.1, 1$ (solid, dashed and dotted lines respectively) in the left panel, and for $\dot{m} = 0.1$, $M_8 = 0.01, 1, 100$ (solid, dashed and dotted lines respectively) in the right panel. The dashed magenta line shows the lower limit for which eq.(64) is valid.

Figure 3 shows m_0 as a function of the radius. On the left panel, we show 3 different cases of accretion rates, $\dot{m} = 0.01, 0.1, 1$, with constant mass $M_8 = 1$, while on the right panel we plot 3 different cases of black hole masses, $M_8 = 0.01, 1, 100$, with constant accretion rate $\dot{m} = 0.1$. With the dashed line we show the lower limit of the parameter space for which eq.(64) is valid. We observe that for all the cases and almost all radii the condition $m_0 \geq 10^3$g cm^{-2} is met. It is also interesting to see that the surface density is independent of the black hole mass in the inner region of the disk.

Figure 4 shows the effective temperature as a function of the radius for the same cases of accretion rates and black hole masses. We can see that the condition $T_{eff} > 10^5$K is satisfied only for cases with high accretion rate and small black hole mass. Moreover, for the cases that it is satisfied, this happens only at the inner part of the disk (for radii smaller than $\sim 50R_g$). This has to be taken into account when calculating the disk spectrum. For example, if we call r_f the radius where $T_{eff} = 10^5$K, then for $r < r_f$ we can use eq.(64) and thus compute the spectrum using the color-corrected blackbody method. At larger radii, however, we need to compute the spectrum using a different method.

Figure 5 shows g as a function of the radius for the same cases of accretion rates and black hole masses as before. We notice that some cases fall outside the parameter space at large radii. However, this seems to happen at radii larger than r_f.

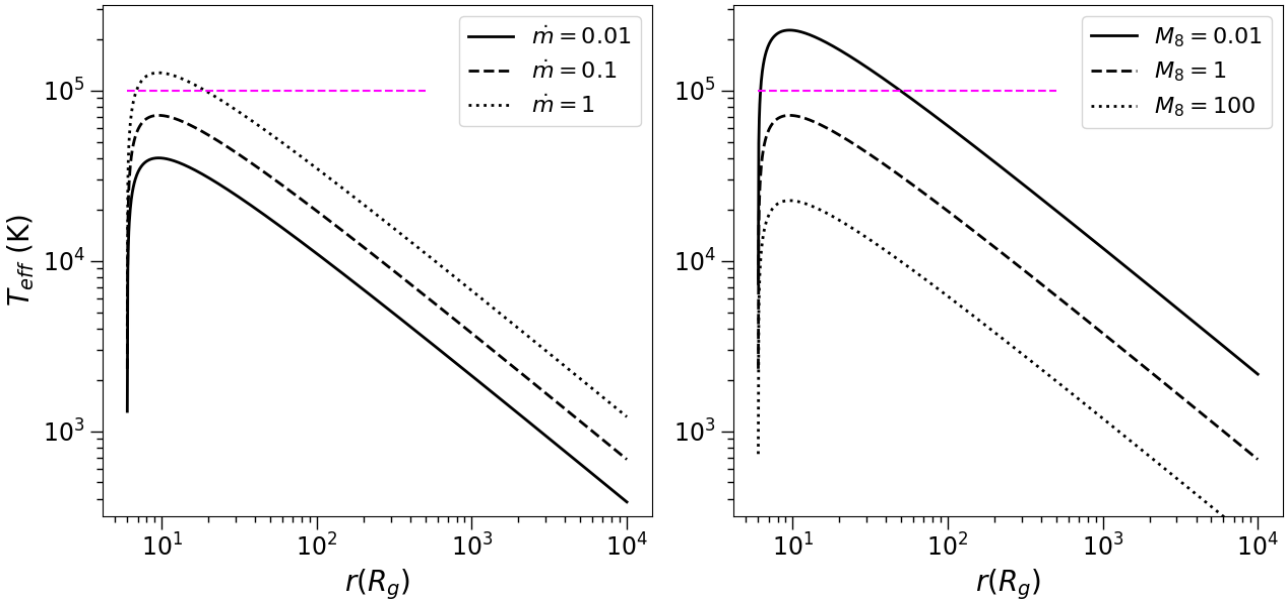

Figure 4: The effective temperature T_{eff} as a function of the radius for black hole mass $M_8 = 1$ and accretion rates $\dot{m} = 0.01, 0.1, 1$ (solid, dashed and dotted lines respectively) in the left panel, and for $\dot{m} = 0.1$, $M_8 = 0.01, 1, 100$ (solid, dashed and dotted lines respectively) in the right panel. The dashed magenta line shows the lower limit for which eq.(64) is valid.

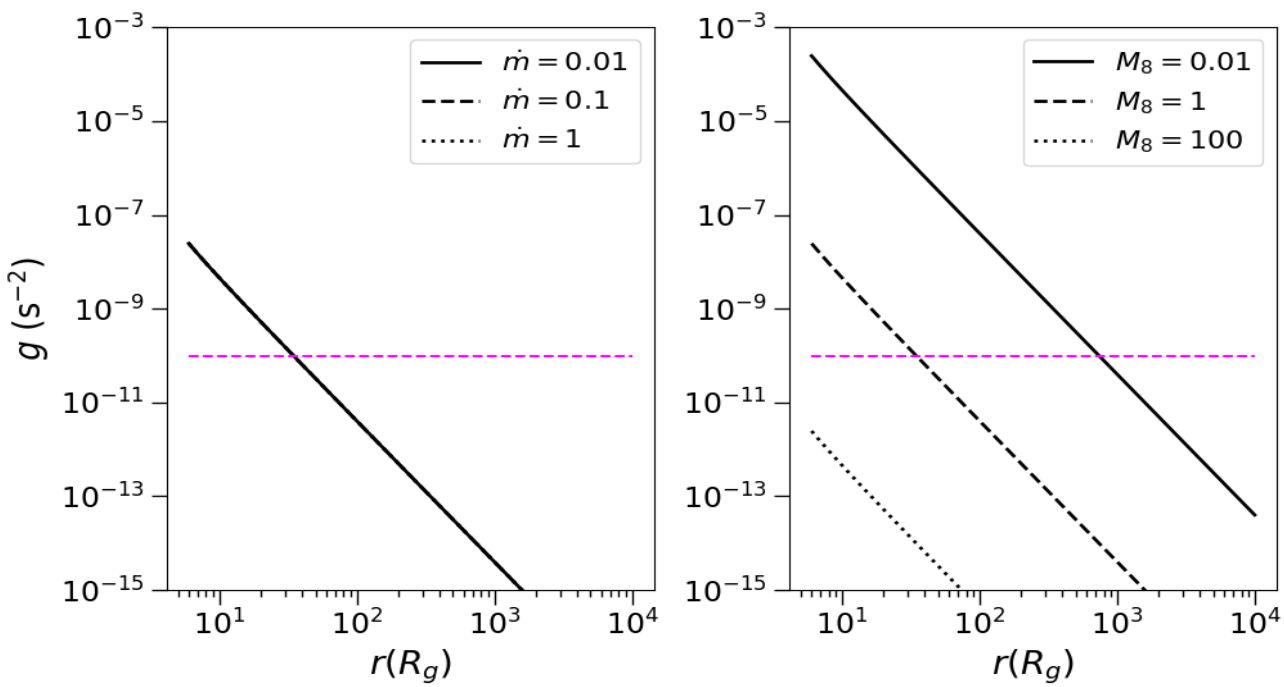

Figure 5: The tidal gravity parameter g as a function of the radius for black hole mass $M_8 = 1$ and accretion rates $\dot{m} = 0.01, 0.1, 1$ (solid, dashed and dotted lines respectively) in the left panel, and for $\dot{m} = 0.1$, $M_8 = 0.01, 1, 100$ (solid, dashed and dotted lines respectively) in the right panel. The dashed magenta line shows the lower limit for which eq.(64) is valid.

3.3 Calculation of the disk spectrum

We consider an accretion disk around a BH of mass M_8, accretion rate $\dot{m}$ (in Eddington units as defined in eq. 9), spin $\alpha^*$and inclination θ. The inner disk radius is the marginably stable orbit

defined in eq.(5), and the outer disk radius is set to $r_{out} = 10000$ (in R_g units). We split the disk radially into 50 rings (with logarithmic step) and azimuthally into 30 parts. In each radius, we can compute the disk parameters ρ, H, T_s using equations of section 2.3 and eq.(59). We can also compute T_{eff}, g, and m_0 using equations (61), (63), and (63). Then, we know all the parameters of the modified blackbody emission and color-corrected blackbody emission, and thus we can calculate the disk spectrum as a function of frequency. We do so for three different cases:

1) we assume that each disk element emits as a blackbody, with specific intensity given by the Planck function defined in eq.(55) (BB model),

2) each disk element emits as a color-corrected blackbody, according to eq.(60), with f being equal to the D12 prescription (D12 model),

3) each disk element emits according to eq.(60) with f computed using the DE19 prescription given in eq.(64), if the T_{eff}, g, and m_0 of the disk element are within the range of values that DE19 considered. If the values of the disk element have not been studied by DE19, the spectrum is assumed to be that of a modified blackbody given in eq.(54) (mBB model).

Having defined the specific intensity $I_\nu(\nu, r)$, one can compute the spectrum in the disk's rest frame as follows:

$$\nu F(\nu) = \int_{r_{ms}}^{r_{out}} \nu I_\nu 2\pi r dr \, (\text{erg s}^{-1}). \tag{65}$$

However, we are interested in the luminosity that is observed at infinity, instead of the local disk luminosity. This calculation is performed by KYN, a set of the XSPEC models for emission from black hole accretion disks, and includes all relativistic effects as detected by an observer at infinity, i.e. gravitational and Doppler shift of the photon energy, gravitational lensing which can amplify the emission from some parts of the disk, etc. (see Dovciak et al. 2004, 2011). It also includes the effects of photons lost to the BH. This way, KYN outputs the flux of the disk as observed at infinity in units of [photons cm^{-2} s^{-1} keV^{-1}]. We then change the units to [erg s^{-1}].

Figure 6 shows the disk spectrum in each emission case for 4 different sets of parameters. In the top left panel, the spectrum was calculated for a black hole of mass $M_8 = 0.01$ and accretion rate $\dot{m} = 0.1$, while in the top right panel, the spectrum was calculated for the same black hole mass and for accretion rate $\dot{m} = 1$. The masses and accretion rates of the bottom left and right panels are $M_8 = 10$, $\dot{m} = 0.1$, $M_8 = 100$, $\dot{m} = 0.1$ respectively. In all panels the black hole spin is $\alpha^* = 0$ and the inclination $\theta = 1^o$. In all computed spectra of this work, the viscosity parameter is $a = 0.1$. The black solid, the blue dashed, and the red dotted lines show models BB, D12, and mBB respectively. For the choice of parameters of the top panels, we find that eq.(64) for f holds at the inner region of the disk. For the top left panel we find $r_f \approx 50$ and for the top right panel $r_f \approx 120$. On the other hand, for the bottom panels eq.(64) does not hold anywhere in the disk, since the effective temperature drops with increasing black hole mass. This means that the red dotted line is calculated using only the modified blackbody method. It is also interesting to see that in the bottom right panel, the BB and D12 cases overlap. This is because the disc temperature is below 3×10^4K at all radii giving $f = 1$, according to the Done et al. formula.

The emission of cases D12 and mBB is shifted to higher frequencies compared with the blackbody emission, as it is expected from the presence of the color-correction factor. Also, from the top panels we see that emission with the D12 prescription is more shifted to higher frequencies than emission from the DE19 formula. However, the bottom panels show that when the disk surface temperature

drops, e.g. for larger black hole masses, the modified blackbody case produces the most emission in high frequencies. This deviation is due to the inclusion of Thomson scattering.

Figure 7 shows the disk spectra for the three different emission cases and for parameters $M_8 = 1$, $\dot{m} = 0.1$, $\theta = 1^o$, and three different spins α^*=0, 0.7, 0.998 (left, center, and right panels respectively). As spin increases the maximum of the luminosity decreases. This is due to the enhanced efficiency that causes the accretion rate in physical units to drop and as a result the total available power for radiation also drops. The spectra, however, extend to slightly higher frequencies as spin increases. This is because r_{ms} moves closer to the black hole where more power is released locally. This causes an increase of the disk temperature at that region.

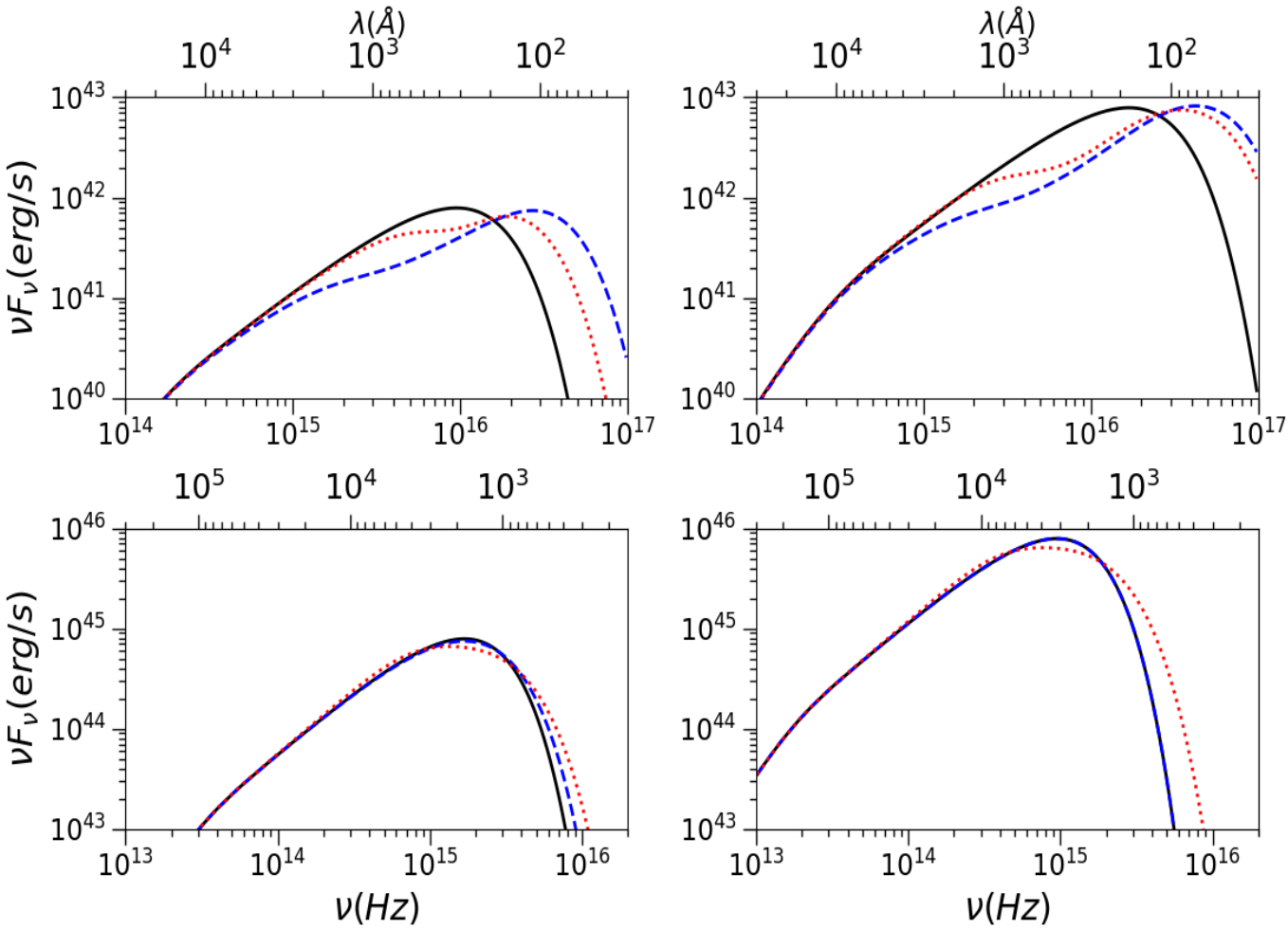

Figure 6: Disk spectra for a $M_8 = 0.01$, $\dot{m} = 0.1$, $M_8 = 0.01$, $\dot{m} = 1$, (top left and right panels respectively) and $M_8 = 10$, $\dot{m} = 0.1$, $M_8 = 100$, $\dot{m} = 0.1$, (bottom left and right panels respectively) for different disk emission assumptions. The spin and inclination are chosen equal to $\alpha^* = 0$, $\theta = 1^o$. The black solid, the blue dashed, and the red dotted lines show models BB, D12, and mBB respectively.

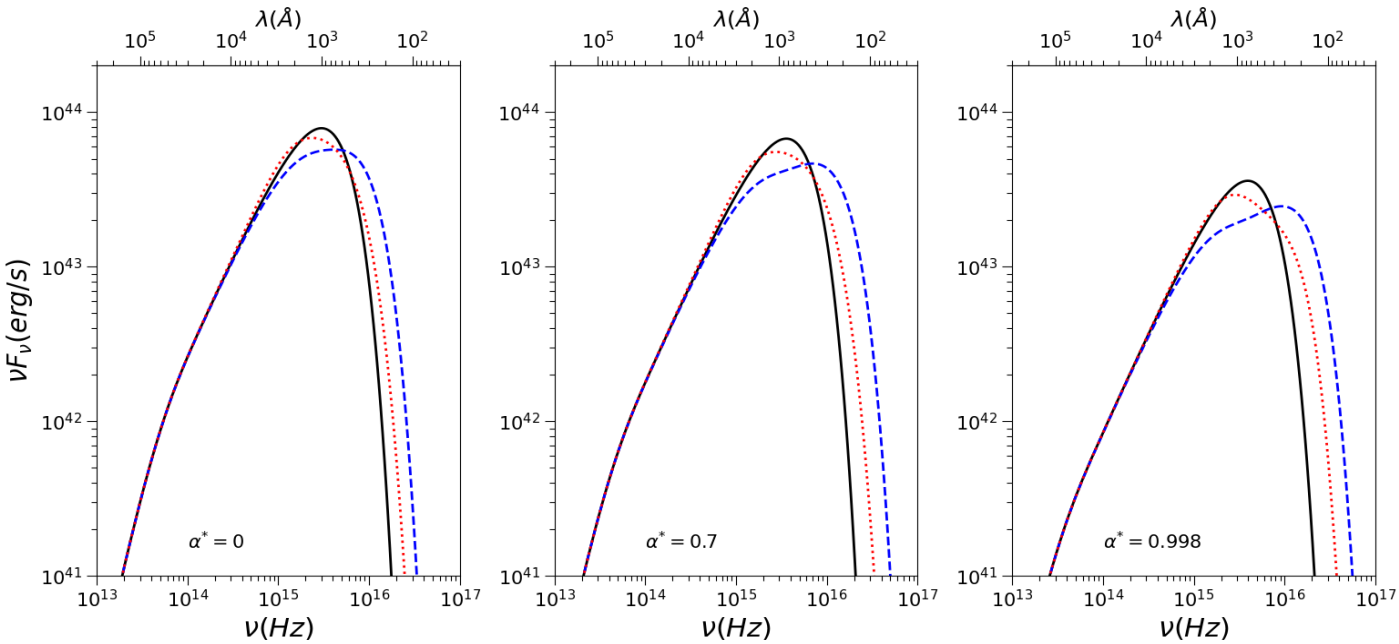

Figure 7: Disk spectra for a $M_8 = 1$, $\dot{m} = 0.1$, $\theta = 1^o$, and spins α^*=0, 0.7, 0.998 (left, center, and right panels respectively), for different disk emission assumptions. The solid black line shows the BB model, the dashed blue line shows the D12 model, and the red dotted line shows the mBB model.

Chapter 4: Fitting the spectral energy distribution of quasars

4.1 The observed AGN SEDs

In this section, we use our model disk spectra to fit the mean spectral energy distribution (SED) of 119,652 quasars that Krawczyk et al. (2013) computed. Their spectra range from infrared to X-ray frequencies, i.e. from 10^{13}Hz to 10^{17}Hz. They included 103,895 quasars from the SDSS-DR7 quasar catalog by Schneider et al. (2010). Since the SDSS survey is limited to relatively bright quasars they also included 15,757 lower luminosity quasars from the Two Degree Field QSO Redshift survey, the Two Degree Field-SDSS LRG and QSO survey and the AAT–UKIDSS–SDSS survey. Mid-infrared data were taken from the WISE final data release (Wright et al. 2010). Data in the near-infrared and optical bands are taken from the Two Micron All Sky Survey (2MASS; Skrutskie et al. 2006) and from the Infrared Deep Sky Survey (UKIDSS; Lawrence et al. 2007). For the UV data they used data from the Galaxy Evolution Explorer (GALEX; Martin et al. 2005). After matching the SDSS sources to the surveys mentioned, they ended up with 85,358 quasars with mid-infrared data, 58,837 quasars with near-IR/optical data, and 42,046 with UV data. In the X-ray band there were only 277 matches to the ChaMP data set (Green et al. 2009), so instead they used a parameterization of the the UV and the X-ray flux to extend their SEDs to X-ray wavelengths.

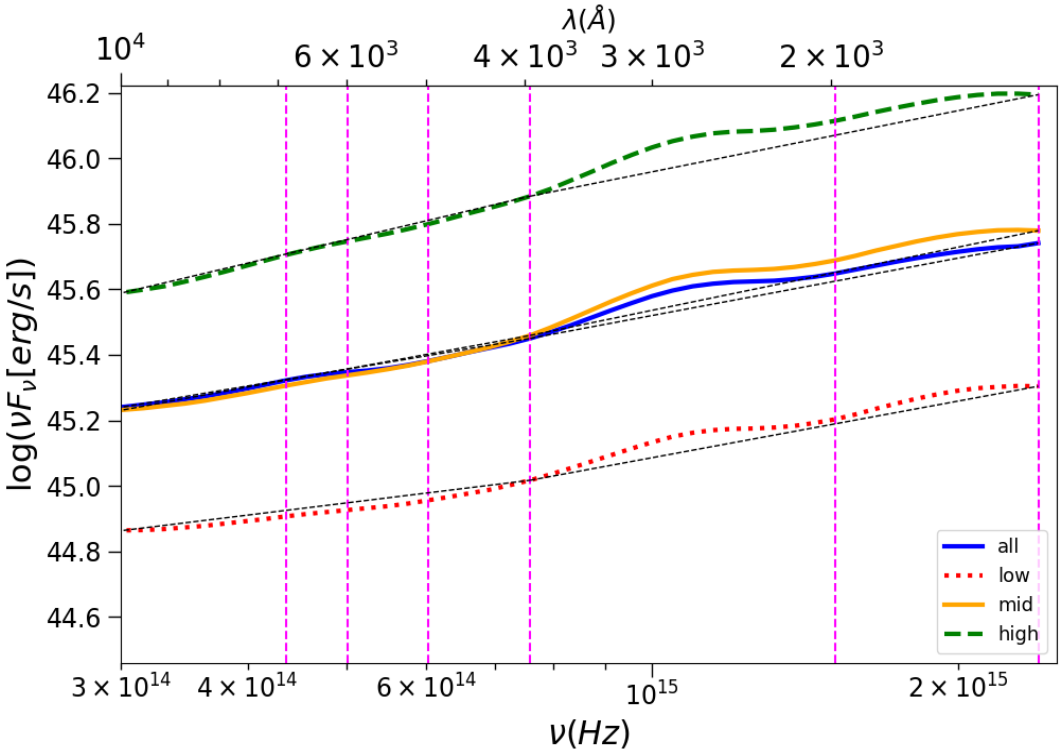

Figure 8: Mean SEDs of low luminosity quasars (red dotted line), mid luminosity quasars (orange solid line), high luminosity quasars (green dashed line) and all quasars (blue solid line) studied by Krawczyk et al. (2013). The vertical dashed lines show the frequencies we considered when fitting the data.

They corrected the observed magnitudes for the contamination of the continuum by emission lines, absorption by intergalactic hydrogen clouds, and host galaxy emission. They also used a "gap filling" SED by looking at the mean SED of ~ 2100 quasars with full wavelength coverage.

Figure 8 shows the corrected SED of Krawczyk et al. (2013) in the frequency range $[2.9 \times 10^{14},\ 2.4 \times 10^{15}]$Hz, i.e. from $\lambda = 1250\mathring{A}$ to $\lambda = 10340\mathring{A}$. The blue solid line shows the mean SED using all quasars, the red dotted line shows the mean SED of the low luminosity quasars (i.e. $\log(\nu F_\nu|_{2500\mathring{A}}) \leq 45.41$), the orange solid line shows the mean SED of the mid luminosity quasars (i.e. $45.41 \leq \log(\nu F_\nu|_{2500\mathring{A}}) \leq 45.85$), and the green dashed line shows the mean SED of the high luminosity quasars (i.e. $\log(\nu F_\nu|_{2500\mathring{A}}) \geq 45.85$), where $\nu F_\nu|_{2500\mathring{A}}$ is measured in erg/s.

The vertical dashed lines of Fig. 8 show the wavelengths we considered when fitting the data with the model SEDs, i.e. $\lambda \approx 7000\mathring{A}, 6000\mathring{A}, 5000\mathring{A}, 4000\mathring{A}, 2000\mathring{A}$, and $1250\mathring{A}$ [3] . For wavelengths smaller than the Lyα line at $1216\mathring{A}$ the number of sources that were used to derive the mean SED drops significantly (see Figure 10 of Krawczyk et al. 2013). Also, emission in larger wavelengths, i.e. mid and far infrared, may originate from dust which is heated by absorbing the AGN UV emission. We therefore considered the broadband SEDs from $7000\mathring{A}$ to $1250\mathring{A}$ as being representative of the continuum emission of quasars. Furthermore, the range $2000\mathring{A} - 4000\mathring{A}$ is also not considered when fitting the data. This is because at that range, FeII emission and the Balmer continuum form a broad and blended feature (known as the "smallblue-bump") which has not been corrected by Krawczyk et al. (2013) and is not modeled by our SEDs.

For each mean data SED, we plot two dashed black lines that connect the wavelengths $10000\mathring{A}$ with $4000\mathring{A}$, let us call its slope $\alpha_{\nu 1}$, and $4000\mathring{A}$ with $1250\mathring{A}$, with slope $\alpha_{\nu 2}$. The luminosity increases with frequency as $L \propto \nu^{\alpha_\nu}$. We calculate the spectral indices α_ν for each data SED and find:

$$\alpha_{\nu 1}^{high} = 0.73\ ,\ \alpha_{\nu 2}^{high} = 0.62\ , \tag{66}$$

$$\alpha_{\nu 1}^{mid} = 0.57\ ,\ \alpha_{\nu 2}^{mid} = 0.64\ , \tag{67}$$

$$\alpha_{\nu 1}^{low} = 0.38\ ,\ \alpha_{\nu 2}^{low} = 0.57\ , \tag{68}$$

$$\alpha_{\nu 1}^{all} = 0.52\ ,\ \alpha_{\nu 2}^{all} = 0.58\ . \tag{69}$$

The steepest SED at large wavelengths (i.e. larger $\alpha_{\nu 1}$) is the high luminosity one, followed by the mid, all, and low luminosity ones respectively. For small wavelengths, the mid luminosity SED is the steepest. We also notice that for the mid, low, and all luminosity SEDs, the slope for small wavelengths is larger than the slope for large ones. This means that as frequency increases the SEDs become more steep. However, the opposite is true for the high luminosity SED.

4.2 Fitting method

Here, we describe the method we use to fit the mean observed SEDs. First, we created model spectra for the three emission cases, described in section 3. We considered 31 M_8 values in the interval [1, 1000] in steps of 0.1 dex, 21 $\dot{m}$ values in [0.01, 1] in steps of 0.1 dex, 3 black hole spin values $\alpha^* = 0, 0.7, 0.998$ and 9 inclination values $\theta = 1^o, 10^o, 20^o, ..., 80^o$. We computed model spectra of all the $M_8, \dot{m}, \alpha^*$, and θ combinations, i.e. we computed a total of 17,577 spectra. Our objective is to find out which combination of model parameters will result to model SEDs whose mean will provide a good fit to the observed data.

To do this we, first, select model SEDs which have spectral slopes similar to the slope of the observed SED at $\lambda < 4000\mathring{A}$. This is done by calculating the ratio of the model luminosities

[3] Krawczyk et al. (2013) computed the mean SEDs for the logarithm of frequencies from 13 to 18.42 with step 0.02, so we use the data points closest to wavelengths mentioned in text which turn out to be $\lambda = 6873\mathring{A}, 5986\mathring{A}, 4979\mathring{A}, 3955\mathring{A}, 1980\mathring{A}$ and $1251\mathring{A}$.

$R_{L,mod} = \left(L_{1250\mathring{A}}\right) / \left(L_{4000\mathring{A}}\right)$ and keeping those with

$$\frac{|R_{L,obs} - R_{L,mod}|}{R_{L,obs}} \leq p \ , \tag{70}$$

where $R_{L,obs}$ is the respective ratio of the observed luminosities, and p is a fitting parameter, $0 < p < 1$. For example, if we choose $p = 0.1$, then since $R_{L,obs} = 2.29$ (for the all luminosity quasars SED), acceptable values of $R_{L,mod}$ are those between 2.06 and 2.52. This process selects the model spectra with a spectral index close to the spectral index of the observed SED. The parameters (M_8, $\dot{m}$, α^*, θ) of each "well-shaped" model SED are saved in an array.

However, the fact that the model SEDs we have selected so far have shapes similar to the shape of the observed SED, does not guarantee that they result to the best-fit. To find the best-fit we continue with the traditional approach of defining a χ^2 function as follows:

$$\chi^2 = \sum_i [\overline{\log(L_{\lambda_i})} - \log(L_{\lambda_i,obs})]^2 \ , \tag{71}$$

where $\overline{\log(L_{\lambda_i})}$ is the mean of the logarithm of the models luminosity at λ_i, and $\log(L_{\lambda_i,obs})$ is the observed luminosity at λ_i (shown in Figure 8). This function measures how well the mean model SED describes the mean observed SED, by computing the squared distance between the data and the model. We will accept as the best-fitting model the model SEDs which will result to the minimum χ^2.

Before we go into minimizing χ^2, we need to calculate the model mean $\overline{\log(L_{\lambda_i})}$. To do this, we create one array for the luminosities of the "well-shaped" model spectra (i.e. the model spectra within each $R_{L,mod} = R_{L,obs}(1 \pm p)$ bin) for each one of the wavelengths $\lambda_i = 7000\mathring{A}, 6000\mathring{A}, 5000\mathring{A}$, $4000\mathring{A}, 2000\mathring{A}$, and $1250\mathring{A}$. Now, we can calculate the mean luminosity at each wavelength as follows:

$$\overline{\log(L_{\lambda_i})} = \frac{1}{N} \sum_{j=1}^{N} \log(L^j_{\lambda_i}) \ , \tag{72}$$

where N is the number of model SEDs within $R_{L,mod} = R_{L,obs}(1 \pm p)$, and $L^j_{\lambda_i}$ is the model luminosity of the j-th SED, at wavelength λ_i. The reason we work with the logarithm of the luminosity and not simply with the luminosity of the model SEDs is because the mean SED of Krawczyk et al. (2013) was computed using the arithmetic mean of $\log(L_\nu)$ (i.e. the geometric mean of L_ν), so to fit their data we need to adopt the same approach.

To minimize χ^2 and choose the appropriate SEDs that will result to the best-fit, we proceed with the following method:

1) We sort the arrays of the model luminosities at each λ_i in order of increasing luminosity at $1250\mathring{A}$. We also apply the same sorting to the array containing the parameters (M_8, $\dot{m}$, α^*, θ) of the model spectra within $R_{L,mod} = R_{L,obs}(1 \pm p)$.

2) We compute the difference dif $= \overline{\log(L_{1250\mathring{A}})} - \log(L_{1250\mathring{A},obs})$. If it is positive, it means that the model SED is above the observed one at that frequency, so we remove the last element of the luminosity arrays. If it is negative, we remove the first element of the arrays. Then we calculate the new χ^2 of the $N_k = N - 1$ model SEDs left. Note that the wavelength λ_i at which dif is computed does not have an important influence on the resulting best fits.

3) We keep removing first/last elements and saving the resulting χ^2 values until $N_k = 1$. Note that we do not recalculate dif, we simply keep removing the first or last elements based on the initial calculation of dif (calculating dif again at each step and then removing the last or the first element of the luminosity arrays results in the same minimum χ^2)

4) We plot χ^2 as a function of N_k and identify the N_k value that minimizes χ^2.

5) By removing the first/last N_k elements of the sorted parameters array, we end up with the parameters that best fit the observed SED. We can then calculate the best fit model SED using these parameters.

We note that computing χ^2 at all available wavelengths, i.e. all data points from 7000$\AA$ to 4000$\AA$ and from 2000$\AA$ to 1250$\AA$ (these are 25 points), did not yield considerable improvement to the best fits, so we use only 6 wavelengths to minimize running times.

The choice of the percentage parameter p significantly influences the best fit derived. For this reason, we perform the above fitting process for p values ranging from 0.1 to 1 with a step equal to 0.05.

The resulting minimum χ^2 and p values of the best-fits are shown in Tables 1, 2 of the next section.

In section 4.3.1, we present the best fits to the all luminosity data SED and the respective distributions of parameters for the three emission cases: BB, D12, and mBB. In section 4.3.2, we fit the low, mid, and high luminosity SEDs.

4.3 Results

4.3.1 Best fits to the mean SED of quasars

Figure 9 shows the best fits and the quasar's overall mean SED (blue solid line). The solid black line shows the best fit when the disk emits as a blackbody (case BB), the black dashed line shows the best fit for the D12 model, while the dotted black line shows the best fit for the mBB model. The minimum χ^2 and the p values which result in the best fits for each model are listed in Table 1 (second and third columns respectively).

Model	χ^2	p
BB	0.012	0.45
D12	0.01	0.25
mBB	0.003	0.1

Table 1: Best-fit values of χ^2 and p for the three models.

We observe that BB and D12 model best-fits are very similar at all frequencies. They are also close to the observed SED at wavelengths between 6000$\AA$ and 1250$\AA$, since the calculation of the χ^2 includes wavelengths between 7000$\AA$ and 1250$\AA$. Interestingly though, the shape of BB and D12 models is not consistent with the observed SED. While the observed SED is more like a power-law increasing towards smaller wavelengths, the model SEDs have a convex shape, with the spectrum showing peak emission at $\sim 1500\AA$ in both cases. Model mBB results in the smallest χ^2 out of the three models, tested here. The mBB SED underestimates the data luminosity, at frequencies larger

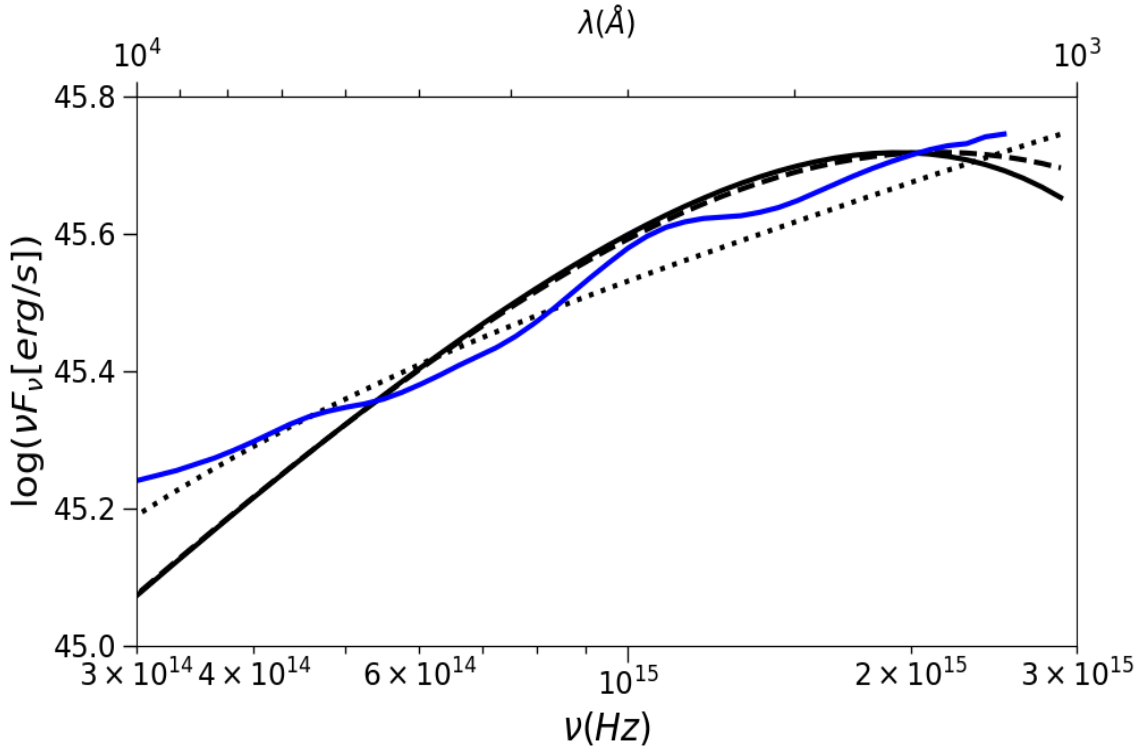

Figure 9: Blue solid line shows the mean quasar SED. The black solid, dashed, and dotted lines indicate the BB, D12, and mBB best fits to the data.

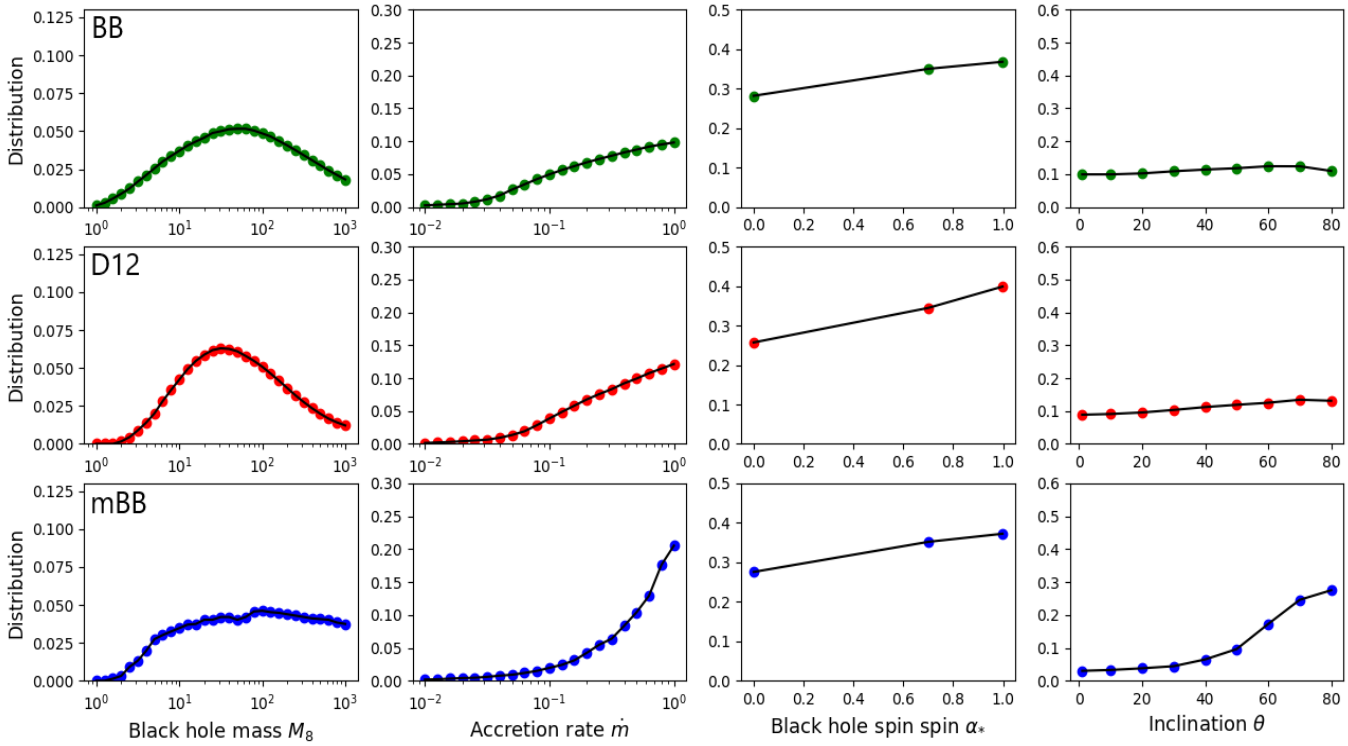

Figure 10: Normalized distributions of the model parameters (M_8, $\dot{m}$, α^*, θ) that provide the model mean SEDs of Figure 9 for BB, D12, and mBB models (top, middle, and lower panels respectively).

that $\sim 10^{15}$Hz, but overall its shape, i.e. the way the luminosity increases with frequency, is very close to the data's SED shape.

Figure 10 shows the distribution of the parameters (M_8, $\dot{m}$, α^*, θ), from left to right, that produce the best fits plotted in Figure 9 (top, middle, and lower panels for BB, D12, and mBB models respectively). The y-axis in each plot shows the normalized distribution of the model spectra, i.e. the number of model spectra at each x-value divided by the total amount of model spectra used to produce the best fit SED.

The black hole mass distribution for the BB model has a peak around $M_8 \sim 50$. The D12 model distribution shows a peak at slightly smaller masses $M_8 \sim 20$. Both distributions fall off at larger masses. However, they do not reach zero, indicating that large BH masses (i.e. $M_8 \sim 1000$) are needed to produce the best fits. The mBB model distributions peaks at even higher BH masses, and does not fall off as quickly as in the other models.

The accretion rate distribution peaks at large accretion rates, in all cases. Low $\dot{m}$ models cannot fit the data. The steepest increase with $\dot{m}$ is observed for the mBB case.

The distribution of the black hole spin is almost identical for all three emission models. Apparently, all spins contribute to a good fit, with large spins being slightly more important. The distribution of the inclination angle is relatively uniform for models BB and D12. However, the case mBB distribution shows a significant increase for large inclinations.

Our results plotted in Figures 9 and 9 indicate that neither model fits well the mean quasar SED. Model mBB does result in a model mean SED which has a shape similar to that of the observed SED, however this is achieved through a rather strange combination of model parameters. If true, then BH masses in quasars should be $\sim 10^{11} M_\odot$ (and even larger) and they should accrete at maximum accretion rates. What is though even more unphysical is the distribution of the inclination angles. Type I objects (like the ones which comprise the sample of Krawczyk et al.) should be seen almost face on. Even if the molecular torus does not exist in luminous quasars, the inclination distribution should be flat. There is no obvious physical reason why we should observe the accretion disk in these objects preferentially edge on.

We repeated the model fits, assuming that the disk inclination is less than 40° in quasars. The results are plotted in Figures 11 and 12.

Figure 11 shows the best fit for each model (like Figure 9) when we assume that we observe the accretion disk with an inclination angle less than 40°. We observe that the deviation of the best fits from the observed SED at high frequencies has increased for the mBB model. Models BB and D12 do not show important changes. In fact, the χ^2 minimum for BB and D12 is almost the same as before, as is listed in Table 2.

Model	χ^2	p
BB	0.012	0.35
D12	0.009	0.15
mBB	0.006	0.1

Table 2: Same as Table 1, when we only consider model spectra with inclinations smaller than 40°.

Figure 12 shows the resulting distribution of the parameters (M_8, $\dot{m}$, α^*, θ). The inclination distribution (rightmost panels) of the mBB model is more uniform than before. The spin distribution is flatter for models BB and D12, when compared with the previous result (when we considered all possible inclinations), as the values at $\alpha^* \sim 1$ have slightly decreased. This trend is maximized for the mBB models where in this case high spin sources should be considerably less common than

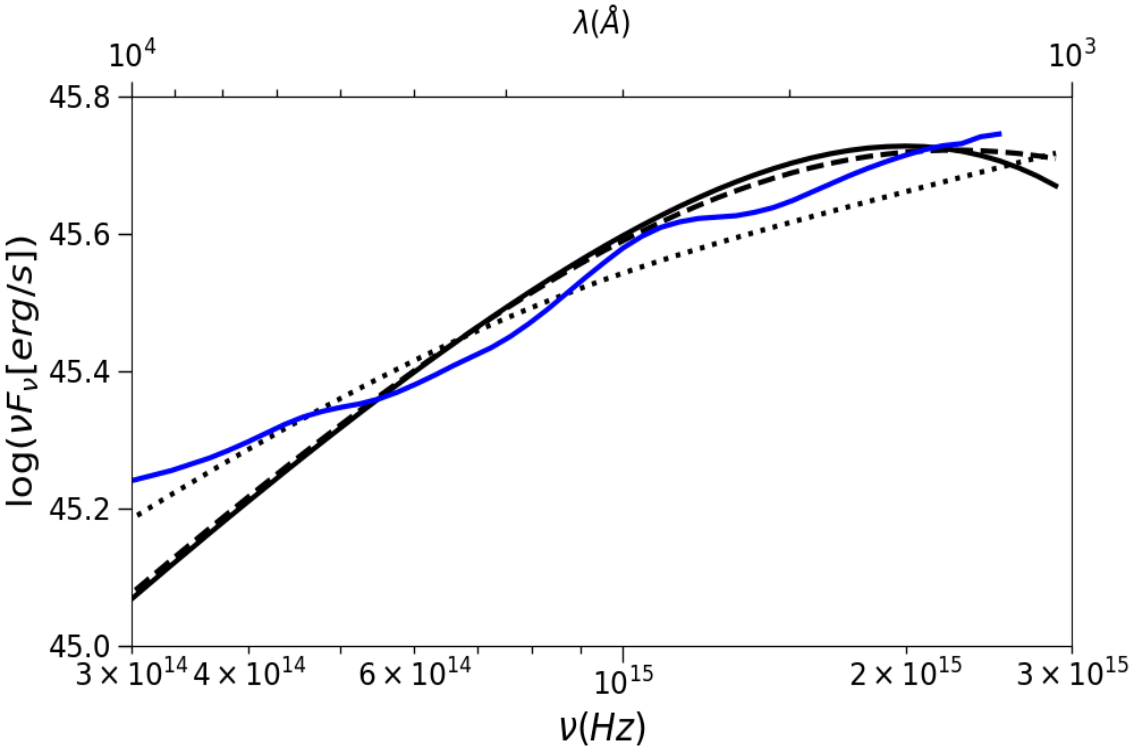

Figure 11: Same as Figure 9, when we assume inclinations angles less than 40°.

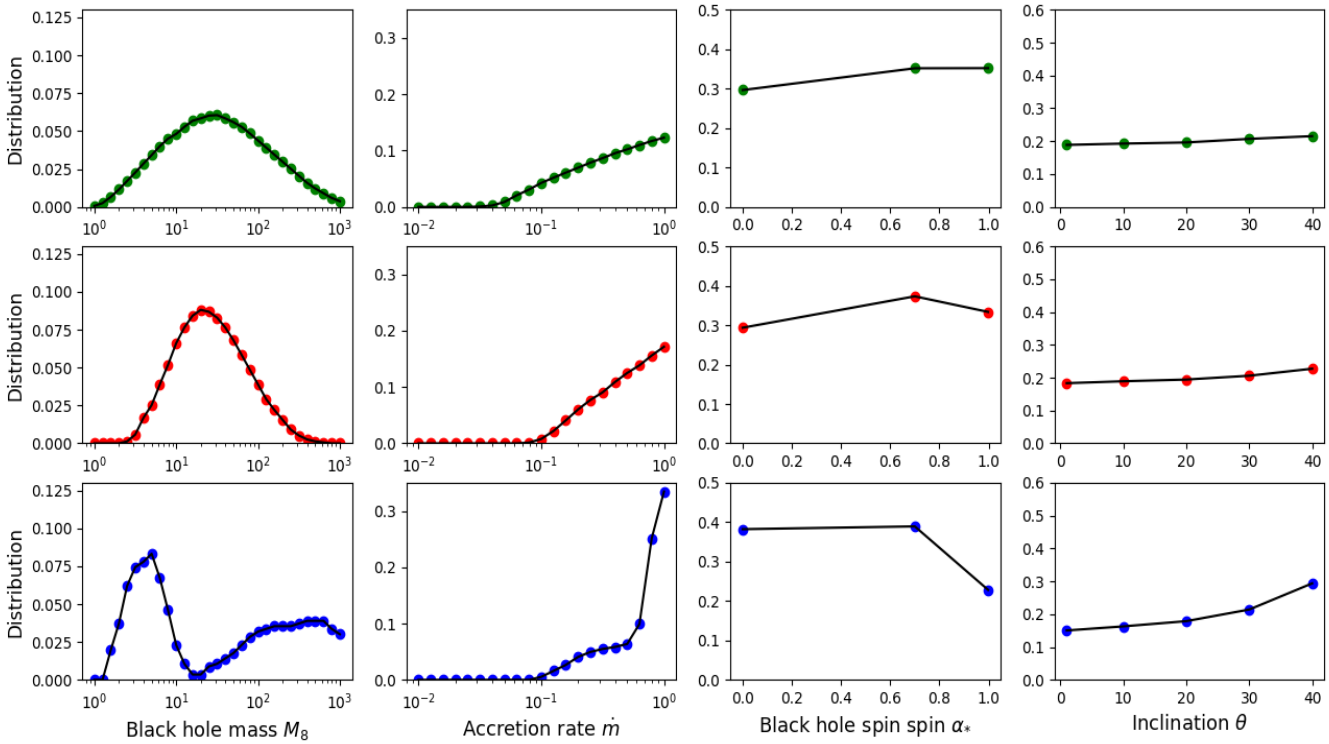

Figure 12: Same as Figure 10, when we assume inclinations angles less than 40°.

sources with small spin. The trend of high accretion rates intensifies in this case for all models. This is even more pronounced in the case of the mBB model. The black hole mass distribution

is not significantly altered for models BB and D12. However, the mBB BH mass distribution is changed. It appears to be bimodal, with a peak between $\sim 10^8 - 10^9 M_\odot$, and then a second peak, but of smaller amplitude, at $\sim 10^{10} - 10^{11} M_\odot$. This mass distribution implies that systems with BH masses in the region $\sim 10^9 M_\odot$, and small inclinations, cannot produce a spectrum with a shape similar to the data's one when the emission is modified blackbody and color-corrected by eq.(64). This feature could be smoothed out by relaxing the constrain that the flux ratio cannot differ more than the best-fitted value of $R_{L,mod}$. However, this would also increase χ^2, i.e. the deviation of the best fit from the data mean SED.

4.3.2 Best fits to the mean SEDs of low, mid, and high luminosity quasars

In addition to fitting the mean SED, we used the same models to fit the observed SED of the low, mid, and high luminosity quasars.

The top, middle, and bottom panels of Figure 13 show the best fits derived when we fit the high, mid, and low luminosity SEDs respectively. Solid, dashed, and dotted black lines show best-fit BB, D12, and mBB models to the observed SEDs.

The top panel shows that BB and D12 models can fit the data well, and in fact better than the mBB case. This is also true for the mid luminosity quasars, as shown in the middle panel. For the low luminosity quasars, the mBB model produces a better fit. This happens because the BB and D12 cases produce a steeper spectrum than the mBB spectrum, and the shape of the mean SED for high and mid luminosity quasars is steeper than the one of the low luminosity quasars.

Figure 14 shows the parameters distribution of the model spectra that produce the best fits plotted in Figure 13. The red dotted, solid orange, and dashed green lines show the distribution we get when we fit the observed mean SED of the low, mid, and high luminosity quasars respectively. The top, middle, and bottom row panels correspond to models BB, D12, and mBB respectively, just like in Figure 9. We observe that all model fits to the high luminosity mean SED require higher BH masses and accretion rates than the fits to the mid and low luminosity ones, as expected. Interestingly, the BH mass distribution of the mBB model does not drop as BH mass increases, but remains almost constant (for $M_8 > 100$).

The distribution of the black hole spins shows a slight increase as spin increases, just like the respective distribution resulting from the model fits to the mean SED of all quasars. The distribution of inclinations for BB and D12 cases is uniform, regardless of the luminosity of the data SEDs (except for a slight increase at 70° for the high and mid luminosities SEDs of the D12 model). The inclination distribution for the mBB model is more uniform when we fit the low luminosity SED. However, the mid and high luminosity AGN can be fitted only with high inclination model spectra, which is hard to understand.

As previously with the mean SED of all quasars, we repeated the fits assuming that we observe quasars with inclination angles less than 40 degrees.

Figure 15 shows the best fits in this case. Its format is the same as that of Figure 13. We notice the mBB model cannot fit the high and mid luminosity SEDs, as before. These spectra can be well fitted by the BB and D12 models (at frequencies larger than $\sim 6 \times 10^{14}$Hz).

Figure 16 shows the distributions of the model parameters that provide the best fit models plotted in Figure 15. Its format is the same as Fig. 14. When compared with the respective distribution in Fig. 14, we observe that the BH, mass distribution is narrower, in the case of models BB and D12, for all luminosity cases. The peak of the distributions does not move. This is not the case though for the mBB model, where the peak of the BH mass distributions shifts to smaller M_8 values. They also get narrower, with a tail that extends to BH masses larger than $\sim 10^9$. We should

keep in mind, though, that this model produces poor fits for high and mid luminosity quasars and thus the resulting distributions are less credible.

The accretion rate distributions are noticeably steeper when we consider inclinations only up to 40°. The black hole spin distributions are roughly uniform for the BB and D12 models. However, the α^*distribution for the mBB model, shows that high spin black holes are less probable, in all luminosity cases. As for the inclination angle distributions, they are uniform, almost for the mBB model as well, contrary to the fits assuming all possible inclinations.

Table 3 lists the best-fit values of χ^2 and p when we fit the low, mid, and high luminosity SEDs using the BB, D12, and mBB models. Table 4 lists χ^2, p when we assume inclinations less than 40 degrees. The χ^2 values confirm that, in general, the BB and D12 models provide better fits for the mid and high luminosity SEDs, while the mBB model can fit the low luminosity SEDs.

Model \ SED	Low	Mid	High
BB	0.016, 0.5	0.007, 0.35	0.004, 0.25
D12	0.014, 0.3	0.006, 0.15	0.003, 0.1
mBB	0.004, 0.1	0.005, 0.1	0.01, 0.1

Table 3: Values of χ^2 and p (in the format χ^2, p) for the best fit of each model (BB, D12, mBB) to the low, mid, and high luminosity quasar observed SEDs.

Model \ SED	Low	Mid	High
BB	0.018, 0.35	0.007, 0.3	0.004, 0.2
D12	0.014, 0.15	0.005, 0.1	0.006, 0.15
mBB	0.006, 0.1	0.019, 0.15	0.029, 0.15

Table 4: Same as Table 3, when we only consider model spectra with inclinations less than 40°.

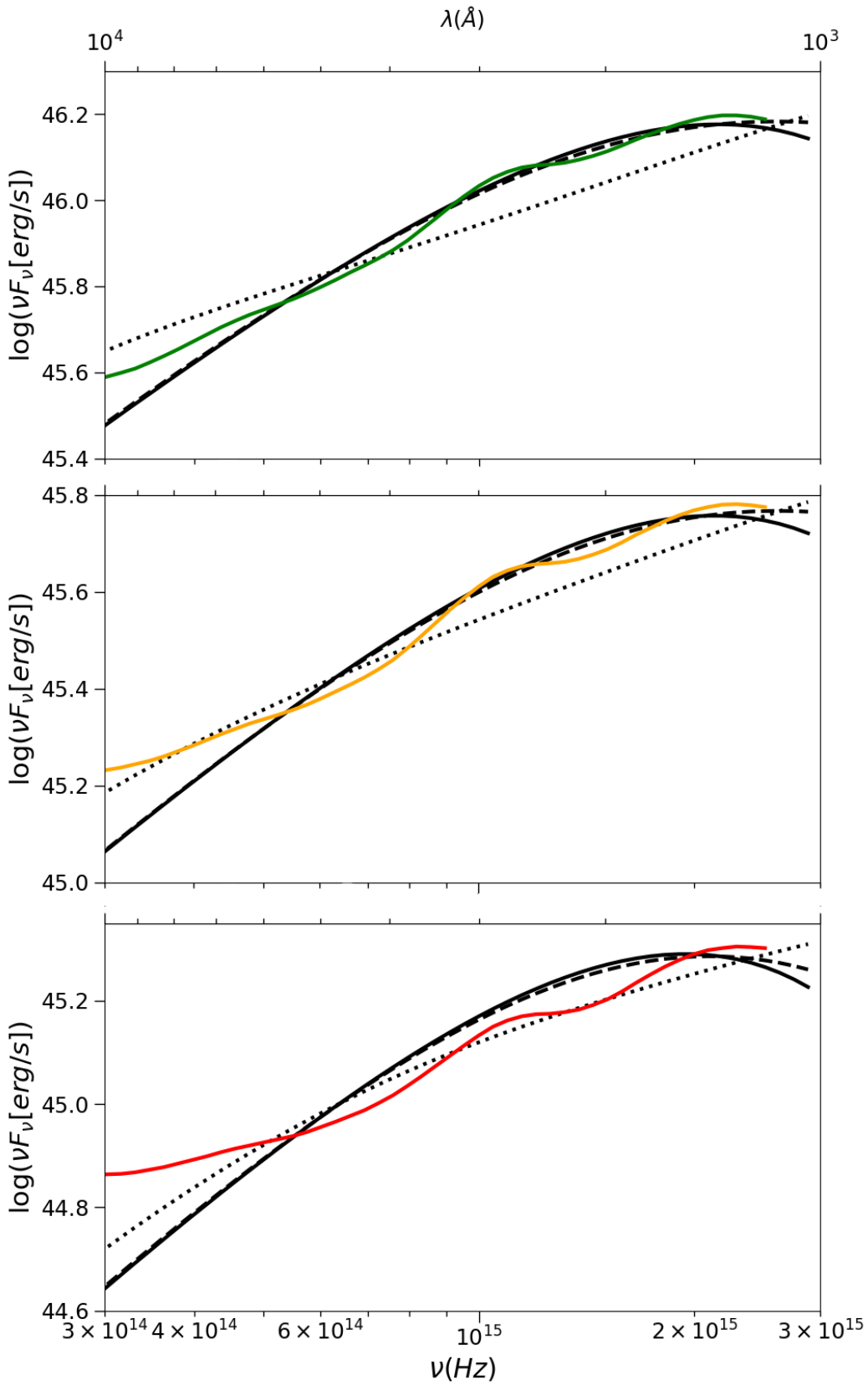

Figure 13: Best fits to the mean SED of the high, mid, and low luminosity quasars (top, middle, and bottom panels respectively) for BB, D12, and mBB models (solid, dashed, and dotted black lines respectively).

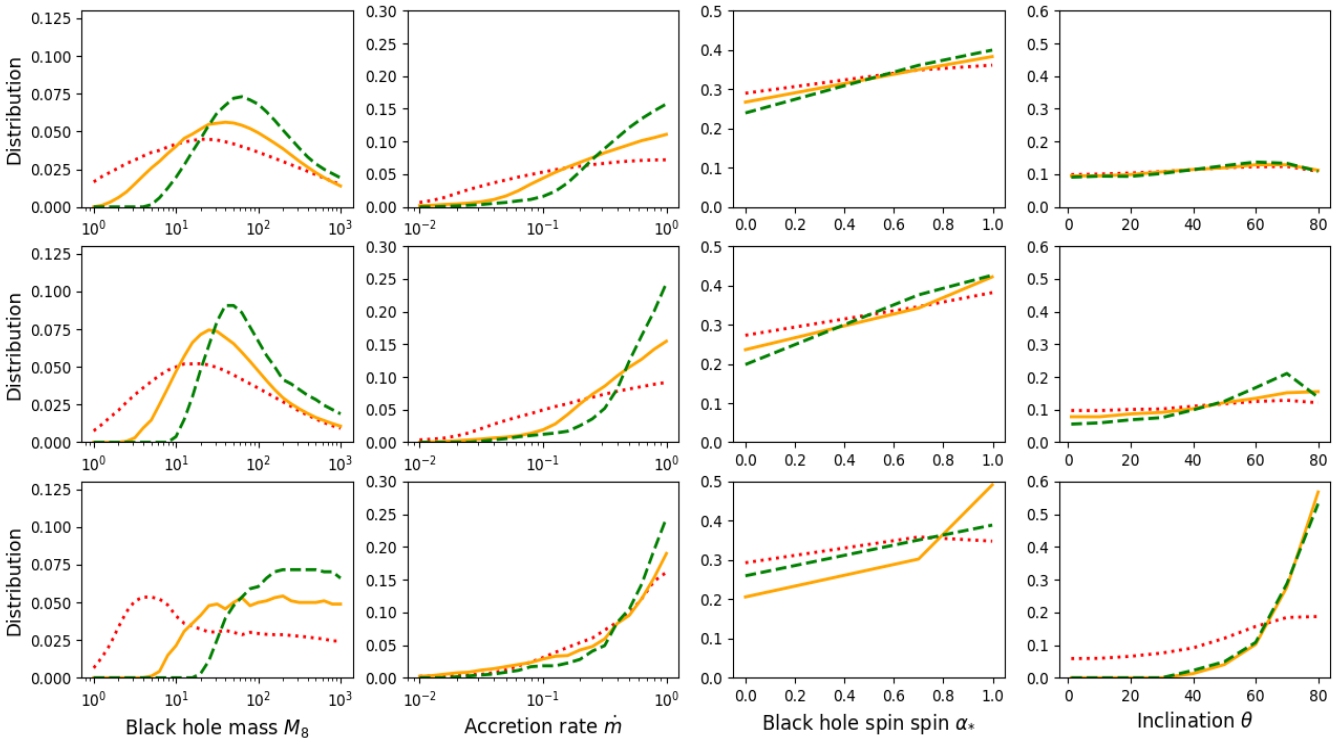

Figure 14: Normalized distribution of the model parameters (M_8, $\dot{m}$, α^*, θ) that produce the best fits plotted in Figure 13. Red dotted lines, orange solid lines, and green dashed lines indicate the model parameter distributions in the case of the model fits to the low, mid, and high luminosity SEDs. The top, middle, and bottom panels show the results for the BB, D12, and mBB models respectively.

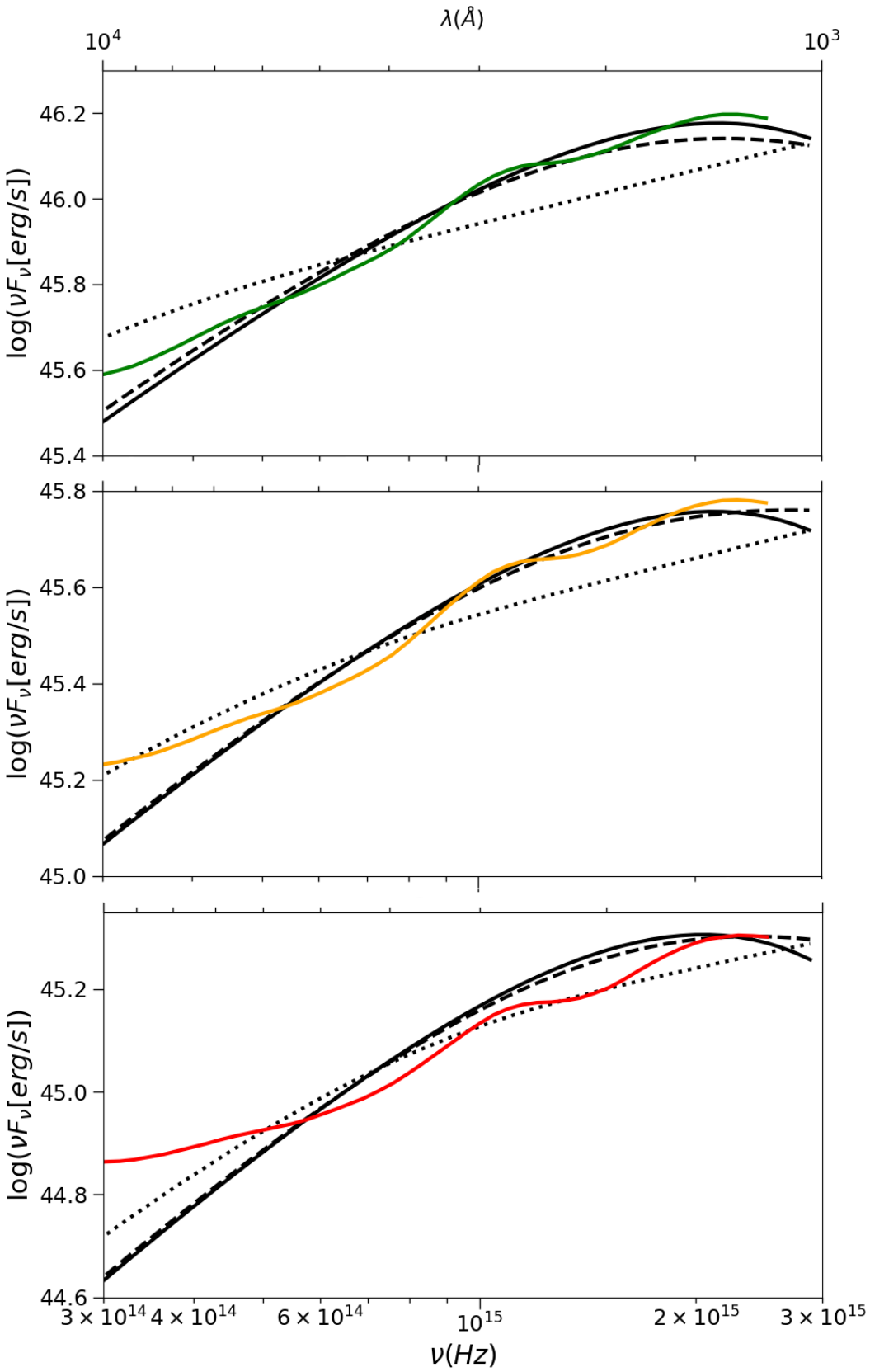

Figure 15: Same as Figure 13, when we assume inclinations angles less than 40°.

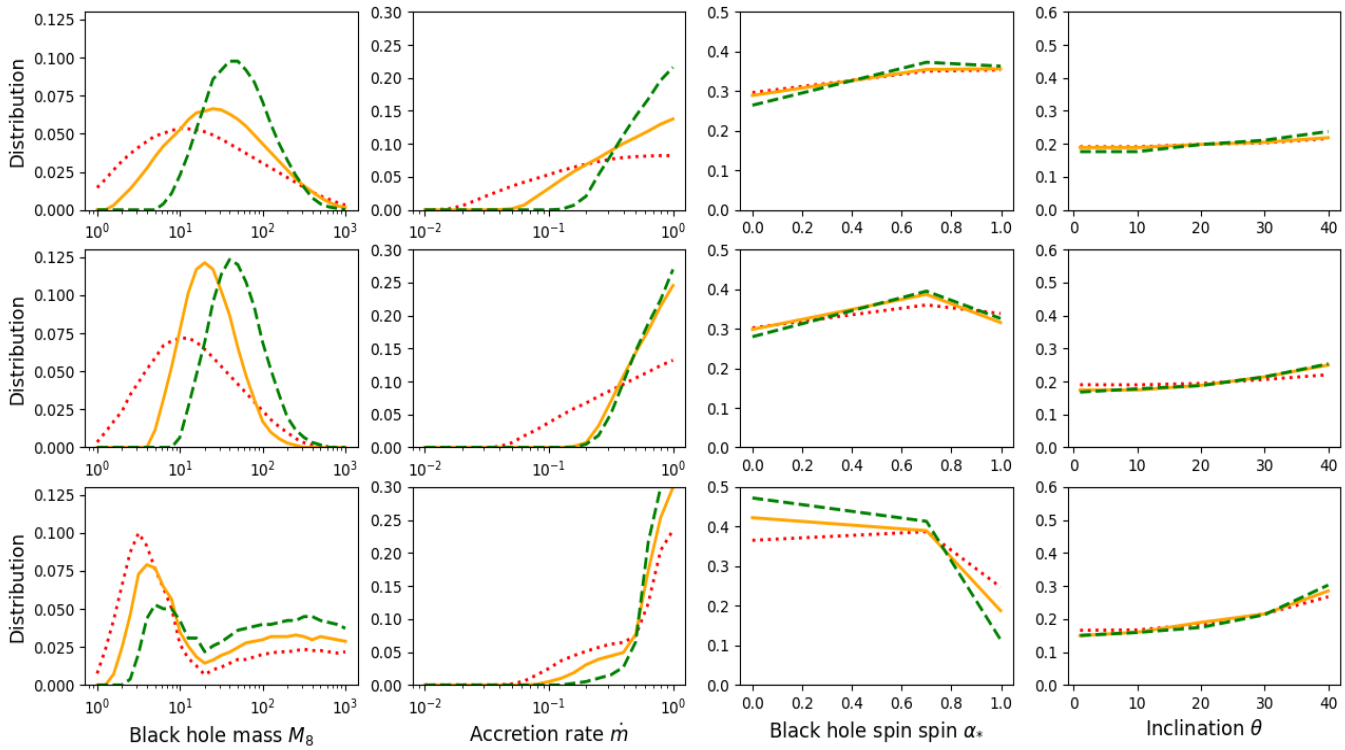

Figure 16: Same as Figure 14, when we assume inclinations angles less than 40°.

Chapter 5: Summary and conclusions

The main objective of this work was to study theoretical models for the spectral energy distribution of accretion disks in AGN, and use these models to fit the observed SEDs of quasars in the optical and UV parts of the spectrum.

In Chapter 2, we first present the equations for the radial and vertical structure of a fully relativistic disk (NT73). Assuming that the disk pressure is due to either radiation pressure or gas pressure, and that the main contribution to opacity originates from either electron scattering or free-free absorption, analytical formulas for the disk parameters (i.e. density, pressure, temperature, height) can be derived.

The calculation of the disk spectrum, which depends on the disk parameters, is performed in Chapter 3. There, we computed the disk spectrum using three different assumptions: A) each disk element emits as a blackbody (BB model), B) each disk element emits as a color-corrected blackbody with spectral hardening factor f given by Done et al. 2012 (D12 model), and C) each disk element emits as a color-corrected blackbody with f given by Davis & El-Abd (2019) and as a modified blackbody in the disk regions where eq. (64) for f is not valid (mBB model). We then used KYNbb, an XSPEC model for emission from black hole accretion disks, to integrate the local flux of the disk and compute the spectrum observed at infinity, including all relativistic effects. We plotted the resulting spectra for different cases of BH mass, accretion rate, and spin.

In Chapter 4, we used the three models for the disk spectrum to fit the observed mean SED of AGN as determined by Krawczyk et al. (2013). To do this, we created 17,577 model spectra (for each one of the BB, D12, and mBB models) for a wide combination of model parameters, i.e. for BH masses $10^8 - 10^{11} M_\odot$, accretion rates $0.01 - 1$, in Eddington units, black hole spins α^*=0, 0.7, 0.998, and inclination angles $1^o - 80^o$. Using the fitting method described in section 4.2, we fit the BB, D12, and mBB model spectra to the observed SED and derive the distribution of model parameters that produce the best-fits. In addition to fitting the mean observed SED of all quasars, given by Krawczyk et al. (2013), we also fit the mean SEDs for low, mid, and high luminosity quasars. Our results can be summarized as follows:

1) The best-fits for the BB and D12 models are very similar, regardless of the luminosity case of the observed SED that we fit. They differ considerably only at frequencies higher than 2×10^{15}Hz, as the D12 model includes the effects of Compton scattering which shift the spectral features at higher frequencies.

2) The mBB model can fit the mean observed SED of all quasars better than the BB and D12 models. However, the best-fit distribution of inclinations implies that most quasars should be observed at inclinations larger than 40 degrees. Although the obscuring torus may be absent in powerful quasars, so we may be able to observe them even at high inclinations, it is highly unlikely that we should preferentially observe them at inclinations larger than 40 degrees. The BB and D12 models produce uniform inclination angle distributions.

3) When we consider model spectra with inclination less than 40 degrees, the mBB model provides a poorer fit to the data, while the BB and D12 model fits remain almost the same. The distribution of inclinations becomes more uniform in the case of the mBB fit, although a peak at inclinations as high as 30-40 degrees is still apparent.

4) The distribution of BH masses in the case of the mBB model fit, both when we assume that we can observe quasars at all inclinations and when we observe them mostly face on, is rather peculiar. In the first case, the BH mass distribution is continuous and peaks at very large

masses ($\sim 10^{10} M_\odot$), with no signs of decreasing even at BH masses as large as $10^{11} M_\odot$. In the second case, the distribution becomes bimodal, with two peaks, one at $\sim 5 \times 10^8 M_\odot$, and a second one at $\sim 5 \times 10^{10} M_\odot$. The BH mass distributions are more reasonable in the case of the BB and D12 models, with smooth, single-peaked distributions which peak at $\sim 10^9 - 10^{10} M_\odot$.

5) The black hole spin distribution for all model best-fits (regardless of the luminosity case of the observed SED) show a slight, but constant, increase as spin increases. However, when we consider only inclinations less than 40°, the spin distribution for the BB and D12 models become more uniform, while the spin distribution for mBB shows a large drop at α^*=0.998.

6) In general, model SEDs with high accretion rates, $\dot{m} > 0.1$, are required to fit the observed SED.

The results change when we consider the model fits to the mean SED of quasars in the low, mid and high luminosity bins. In this case, the BB and D12 models appear to fit the mid and high luminosity mean SEDs better than the mBB model, at least at wavelengths shorter than $\sim 6000\mathring{A}$. On the other hand, the mBB model appears to provide a better fit to the low luminosity SED. The above results hold both in the case when we assume that we can observe quasars with inclinations up to 80 degrees or up to 40 degrees. The distributions of the best-fit model parameters are similar to the distributions of the respective model parameters from the fits to the mean SED of all quasars. Ragarding the fits to the mid and high luminosity SEDs, the results indicate reasonable BH mass distributions and quasars with high spin black holes and high accretion rates.

The fact that the BB model can fit the mid and high luminosity SEDs is rather unexpected. We would not expect that result since the effects of electron scattering should be more important for those objects, and the blackbody model does not consider them. This is an indication that the model fits the data by chance. This conclusion is reinforced by the fact that the low luminosity SED is not fitted well by the BB model. In this case, the mBB model fits the data well, but for an unreasonable distribution of inclinations. This distribution becomes more reasonable if we assume that we cannot observe AGN at inclinations larger than 40 degrees. In this case, the mBB model fits predict significantly smaller number of quasars with high spin and accretion rates smaller than 0.1. It is even more strange that the best-fit predicts a long tail at high BH masses which is rather arbitrary.

It is clear that there is difficulty in fitting well the observed data. We could accept that the D12 model is giving a good fit to the mid and high luminosity SEDs with resulting parameter distributions that are not unphysical. It cannot, however, fit the low luminosity and the overall luminosity mean SEDs. These SEDs are well-fitted by the mBB model but for unreasonable distribution of parameters.

There are various possibilities of proceeding further. For example, one could consider effects of intrinsic absorption in quasars, or consider a different accretion disk model, taking into account the interaction between the disk and the X-ray source in AGN. In this case, one could create model SEDs using models that include the illumination of the accretion disk by the X-ray source, and take into account the mutual interaction of the disk and the corona. A model that takes into account X-ray illumination of the disk in AGN is KYNSED (Dovciak et al. 2022). KYNSED models the interaction between the disk and the Xray source in the case when the X-ray source is powered by the accretion process. Fitting the observed SEDs with models that include these effects for a wide range of mass, accretion rate, spin, inclination and possibly other parameters (location of the corona, accretion power transferred to the corona) could be an interesting prospect to follow.

Appendices

Appendix A: Derivation of disk's inner region parameters

In the inner region the pressure is given by

$$P = P_{rad} = \frac{4\sigma T^4}{3c} \tag{73}$$

and the opacity is equal to the electron scattering opacity, $\kappa_R = \kappa_{es}$. From the energy balance equation we know that

$$F = \frac{Q_{GR}}{2} \ . \tag{74}$$

We substitute the disk flux, F, using eq.(33) and the power per unit surface area due to accretion, Q_{GR}, from eq.(1), into the energy balance equation. We find

$$\frac{4\sigma}{3\rho H \kappa_{es}} T^4 = \frac{1}{2}\frac{3}{8\pi}\frac{GM\dot{M}}{R^3}\frac{\mathcal{L}}{\mathscr{B}\mathscr{C}^{1/2}} \ . \tag{75}$$

Next, we use eq.(73) to substitute the temperature. This leads to the following equation between the disk height, pressure and density:

$$\frac{c}{\rho H \kappa_{es}} P = \frac{1}{2}\frac{3}{8\pi}\frac{GM\dot{M}}{R^3}\frac{\mathcal{L}}{\mathscr{B}\mathscr{C}^{1/2}} \ . \tag{76}$$

We substitute the pressure from eq.(31) and notice that the density cancels out. This means that we have an equation that can be solved for the disk height as shown below

$$\frac{c}{\rho H \kappa_{es}} \rho \frac{GM}{R^3} H^2 \frac{\mathscr{B}^2 \mathscr{D} \mathscr{E}}{\mathscr{A}^2 \mathscr{C}} = \frac{1}{2}\frac{3}{8\pi}\frac{GM\dot{M}}{R^3}\frac{\mathcal{L}}{\mathscr{B}\mathscr{C}^{1/2}} \Rightarrow H = \frac{1}{2}\frac{3}{8\pi}\frac{\kappa_{es}}{c}\dot{M}\frac{\mathscr{A}^2\mathscr{C}^{1/2}\mathcal{L}}{\mathscr{B}^3\mathscr{D}\mathscr{E}} \ . \tag{77}$$

We can proceed to find expressions for the rest of the unknowns quantities. Using again the energy balance equation, but substituting Q_{GR} from eq.(32), we get

$$\frac{4\sigma}{3\rho H \kappa_{es}} T^4 = \frac{3}{2} a \left(\frac{GM}{R^3}\right)^{1/2} H P \frac{\mathscr{D}}{\mathscr{C}} \ . \tag{78}$$

We substitute the temperature from eq.(75) and then we use eq.(31) for the pressure. This leads to an equation between the height and the density that can be solved for the density

$$\rho = \frac{2c}{3a\kappa_{es}} \left(\frac{GM}{R^3}\right)^{-1/2} H^{-2} \frac{\mathscr{C}}{\mathscr{D}} \ . \tag{79}$$

Using eq.(77) for the height we find the disk density

$$\rho = \left(\frac{8\pi}{3}\right)^2 \frac{c^3}{6a\kappa_{es}^3} \left(\frac{GM}{R^3}\right)^{-1/2} \dot{M}^{-2} \frac{\mathscr{B}^6 \mathscr{D} \mathscr{E}^2}{\mathscr{A}^4 \mathcal{L}^2} \ . \tag{80}$$

We can substitute eq.(80) and eq.(77) into eq.(31) to find the pressure. And lastly, calculate the temperature from eq.(73).

It is also useful to see how we can turn eq.(77) for the height into the form of eq.(36). To do this we make the change of variables from $R, M, \dot{M}$ to the dimensionless quantities

$$r = \frac{R}{R_g} \ , \ M_8 = \frac{M}{10^8 M_\odot} \ , \ \dot{m} = \frac{\eta \dot{M} c^2}{L_{edd}} \ , \tag{81}$$

where L_{edd} is the Eddington luminosity given by

$$L_{edd} = 1.26 \times 10^{38} \frac{M}{M_\odot} \ (\text{erg/sec}) \ , \tag{82}$$

The above definitions lead to the substitutions

$$R = rR_g = r\frac{GM}{c^2} = 10^8 \frac{GM_\odot}{c^2} r M_8 = (1.5 \times 10^{13}\text{cm}) r M_8 \ , \tag{83}$$

$$M = 10^8 M_\odot M_8 = (2 \times 10^{41}\text{g}) M_8 \ , \tag{84}$$

$$\dot{M} = \frac{\dot{m}}{\eta}\frac{L_{edd}}{c^2} = \frac{1.26 \times 10^{46}}{c^2}\frac{\dot{m}}{\eta} M_8 = (1.4 \times 10^{25}\text{g/s})\frac{\dot{m}}{\eta} M_8 \ , \tag{85}$$

where we used $G = 6.67 \times 10^{-8}\text{cm}^3\text{g}^{-1}\text{s}^{-2}$, $M_\odot = 2 \times 10^{33}$g and $c = 3 \times 10^{10}$ cm s^{-1}. We can now calculate the ratio H/R

$$\frac{H}{R} = \frac{1}{2}\frac{3}{8\pi}\frac{\kappa_{es}}{c}\frac{\dot{M}}{R}\frac{\mathscr{A}^2\mathscr{C}^{1/2}\mathcal{L}}{\mathscr{B}^3\mathscr{D}\mathscr{E}} = \frac{1}{2}\frac{3}{8\pi}\frac{\kappa_{es}}{c}\frac{(1.4 \times 10^{25}\text{g/s})}{(1.5 \times 10^{13}\text{cm})}\frac{\dot{m}}{\eta} r^{-1}\frac{\mathscr{A}^2\mathscr{C}^{1/2}\mathcal{L}}{\mathscr{B}^3\mathscr{D}\mathscr{E}} \Rightarrow \tag{86}$$

$$\frac{H}{R} \approx \frac{\dot{m}}{\eta} r^{-1}\mathscr{A}^2\mathscr{B}^{-3}\mathscr{C}^{1/2}\mathscr{D}^{-1}\mathscr{E}^{-1}\mathcal{L}^1 \ . \tag{87}$$

Similarly, one can derive the rest of the disk parameters for all regions.

Appendix B: Computation of disk's surface temperature

To calculate the surface temperature of the disk we follow the steps below:

1. we split the disk into 50 annuli (each annulus has an inner radius r_i and an outer radius r_{i+1}), using eq.(13),

2. we solve eqs.(40) and (46) numerically to find the transition radii,

3. we solve eq.(59) numerically for each radius r_i, using the Newton-Raphson method. To do this, one must calculate the expression

$$4\pi\frac{k^4 T_s^4(r)}{h^3 c^2}\int_0^\infty \frac{x^3 dx}{(e^x - 1)[1 + \sqrt{1 + \kappa_{es}/\kappa_{ff}(x, \rho(r), T_s(r))}]} - 7 \times 10^{18}\frac{\dot{m}}{M_8} r^{-3}\frac{\mathcal{L}}{\mathscr{B}\mathscr{C}^{1/2}} \ , \tag{88}$$

and its derivative with respect to T_s. The integral of the above expression is computed over the interval $[0.01, 30]$ using the trapezoidal rule, i.e.

$$\int_0^\infty f(x)dx \approx \int_{0.01}^{30} f(x)dx = \sum_{i=0}^{N}\frac{f(x_{i+1}) + f(x_i)}{2}\Delta x_i \ , \tag{89}$$

where $\Delta x_i = x_{i+1} - x_i$ and

$$f(x) = \frac{x^3}{(e^x - 1)(1 + \sqrt{1 + \kappa_{es}/\kappa_{ff}(x, \rho, T_s)}} \ . \tag{90}$$

In our case, N=99, and the points x_i are calculated by $\log(x_i) = \log(x_{low}) + i[\log(x_{high}) - \log(x_{low})]/100$, with $x_{low} = 0.01$ and $x_{high} = 30$. We note that $f(x)$ falls off very quickly for very small and large x, and it is for this reason that the interval $[0.01, 30]$ is a good approximation of $[0, \infty]$. The function $f(x)$ also depends on κ_{ff} and therefore the disk density. At radii $r_i < r_1$ we compute the density using eq.(35), at radii $r_1 < r_i < r_2$ we use eq.(41), while for $r_i > r_2$ we use eq.(47).

Bibliography

Abramowicz, M.A. and Fragile, P.C., 2013. Foundations of black hole accretion disk theory. Living Reviews in Relativity, 16, pp.1-88.

Bardeen, J.M., Press, W.H. and Teukolsky, S.A., 1972. Rotating black holes: locally nonrotating frames, energy extraction, and scalar synchrotron radiation. Astrophysical Journal, Vol. 178, pp. 347-370 (1972), 178, pp.347-370.

Capellupo, D.M., Netzer, H., Lira, P., Trakhtenbrot, B. and Mejía-Restrepo, J., 2015. Active galactic nuclei at z 1.5–I. Spectral energy distribution and accretion discs. Monthly Notices of the Royal Astronomical Society, 446(4), pp.3427-3446.

Carroll B. W., Ostlie D. A, 2007, "An Introduction to Modern Astrophysics", 2nd ed., Pearson Addison-Wesley

Czerny B. & Naddaf M. H., 2019, "Accretion in Active Galactic Nuclei", PoS

Dominik C., 2015, "Disk formation and structure", EPJ Web of Conferences, Vol.102, 00002

Davis, S.W. and El-Abd, S., 2019. Spectral Hardening in Black Hole Accretion: Giving Spectral Modelers an f. The Astrophysical Journal, 874(1), p.23.

Done, C., Davis, S.W., Jin, C., Blaes, O. and Ward, M., 2012. Intrinsic disc emission and the soft X-ray excess in active galactic nuclei. Monthly Notices of the Royal Astronomical Society, 420(3), pp.1848-1860.

Dovciak, M., 2004. Radiation of accretion discs in strong gravity. arXiv preprint astro-ph/0411605.

Dovčiak, M., Papadakis, I.E., Kammoun, E.S. and Zhang, W., 2022. Physical model for the broadband energy spectrum of X-ray illuminated accretion discs: Fitting the spectral energy distribution of NGC 5548. Astronomy & Astrophysics, 661, p.A135.

Frank J, King A., Raine D., 1992, "Accretion Power in Astrophysics", 2nd ed., Cambridge University Press

Hubeny, I. and Hubeny, V., 1997. Non-LTE models and theoretical spectra of accretion disks in active galactic nuclei. The Astrophysical Journal, 484(1), p.L37.

Madej, J., 1974. Influence of scattering on the continuous spectrum emitted by the grey atmosphere-Approximate solution. Acta Astronomica, vol. 24, no. 4, 1974, p. 327-336., 24, pp.327-336.

Mehdipour, M., Kaastra, J.S., Kriss, G.A., Cappi, M.A.S.S.I.M.O., Petrucci, P.O., Steenbrugge, K.C., Arav, N., Behar, E., Bianchi, S., Boissay, R. and Branduardi-Raymont, G., 2015. Anatomy of the AGN in NGC 5548-I. A global model for the broadband spectral energy distribution. Astronomy Astrophysics, 575, p.A22.

Novikov, I.D. and Thorne, K.S., 1973. Astrophysics of black holes. Black holes (Les astres occlus), 1, pp.343-450.

Koratkar, A. and Blaes, O., 1999. The ultraviolet and optical continuum emission in active galactic nuclei: the status of accretion disks. Publications of the Astronomical Society of the Pacific, 111(755), p.1.

Krawczyk, C.M., Richards, G.T., Mehta, S.S., Vogeley, M.S., Gallagher, S.C., Leighly, K.M.,

Ross, N.P. and Schneider, D.P., 2013. Mean spectral energy distributions and bolometric corrections for luminous quasars. The Astrophysical Journal Supplement Series, 206(1), p.4.

Page, D.N. and Thorne, K.S., 1974. Disk-accretion onto a black hole. Time-averaged structure of accretion disk. The Astrophysical Journal, 191, pp.499-506.

Pariev V. I., Blackman E. G. & Boldyrev S. A., 2003, "Extending the Shakura-Sunyaev approach to a strongly magnetized accretion disc model", A&A, Vol.407, p.403

Peterson B. M, 1997, "An Introduction to Active Galactic Nuclei", Cambridge University Press

Pringle J. E., 1981, "Accretion Discs in Astrophysics", ARA&A, Vol.19, p.137

Riffert, H. and Herold, H., 1995. Relativistic accretion disk structure revisited. Astrophysical Journal v. 450, p. 508, 450, p.508.

Rybicki, G. B., & Lightman, A. P. 1979, "Radiative Processes in Astrophysics", New York: John Wiley

Sadowski A., Lasota J. P., Abramowicz M. A. & Narayan R., 2016, "Energy flows in thick accretion discs and their consequences for black hole feedback", MNRAS, Vol.456, p.3915 Pringle J. E., 1981, "Accretion Discs in Astrophysics", ARA&A, Vol.19, p.137

Shakura, N. I. & Sunyaev, R. A., 1973, "Black holes in binary systems. Observational appearance", A&A, Vol.24, p.337

Shimura, T. and Takahara, F., 1995. On the spectral hardening factor of the X-ray emission from accretion disks in black hole candidates. The Astrophysical Journal, 445, pp.780-788.

Svensson, R. & Zdziarski, A. A., 1994, "Black hole accretion disks with coronae", ApJ, Vol.436, p.599

Zimmerman E. R., Narayan R., McClintock J. E. & Miller J. M., 2004, "Multi-Temperature Blackbody Spectra of Thin Accretion Disks With and Without a Zero-Torque Inner Boundary Condition", ApJ, Vol.618, p.832